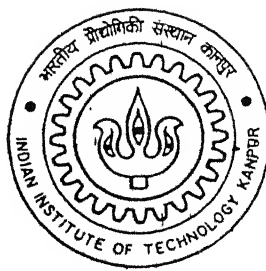# Enhancement of Heat Transfer Using Oval Tube and Vortex Generators

By

DALTON MAURYA

DEPARTMENT OF MECHANICAL ENGINEERING

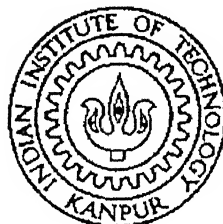# Indian Institute of Technology Kanpur
NOVEMBER, 2001

Enhancement of Heat Transfer Using Oval Tube and Vortex Generators

*A Thesis Submitted
in partial Fulfillment of the requirements
for the Degree of*

MASTER OF TECHNOLOGY

by

DALTON MAURYA

**DEPARTMENT OF MECHANICAL ENGINEERING
INDIAN INSTITUTE OF TECHNOLOGY , KANPUR**

November, 2001

Certificate

This is to certify that the thesis entitled **"Enhancement of Heat Transfer using Oval Tube and Vortex Generators"** by Mr. Dalton Maurya has been carried out under my supervision. The contents of this thesis have not been submitted to any other institute or university for the award of any degree or diploma.

Dr. Gautam Biswas

Professor

Department of Mechanical Engineering

Indian Institute of Technology

Kanpur-208016

November 28, 2001

ABSTRACT

Three-dimensional flow and heat transfer in a channel with a built-in oval tube and delta winglets have been computed through the solution of complete Navier-Stokes and energy equations using a body-fitted grid and a Finite-Volume Method. The geometrical configuration represents an element of a gas-liquid fin-tube cross flow heat exchanger. The gas side heat transfer coefficient is usually small as compared to the liquid side. The air-cooled condensers of the geothermal power plants also use fin-tube heat exchangers. The size of the condensers is huge and at the same time the cost is about one-third of the plant cost. A strategy has been evolved in order to reduce the size of such heat exchangers through enhancement in transport coefficients on the air (gas) side. At the first place, oval tubes are suggested in place of circular tubes. In a subsequent move, the delta winglet type vortex generators in common-flow-down configuration are recommended to be mounted on the fin-surface in front of the tube. Finally, another delta winglet pair in common-flow-up configuration is suggested to be mounted in downstream of the first winglet pair. A detailed evaluation of the augmentation strategy has been accomplished in this investigation. The investigation was carried out for three angles of attack ($\beta = 30^0$, 35^0, and 40^0) of the winglets and three different Reynolds numbers (Re = 500, 1000, and 1500). The structures of the velocity field, and the heat transfer characteristics have been presented. Results show remarkable promise of the vortex generators in conjunction with the oval tube as an improvement device.

ACKNOWLEDGEMENTS

CONTENTS

4   Results and Discussion

5   Conclusion and Scope for Future Work

List of Figures

List of Tables

NOMENCLATURE

a   semi major diameter

b   semi minor diameter

B   channel width

CV   control volume

F   mass flux through a cell face

H   channel height

k   thermal conductivity of the fluid

Nu   local Nusselt number, $\dfrac{1}{(1-\theta_b)}\left\{\dfrac{\partial \theta}{\partial Z}\right\}_{Z=w}$

Nu_m Mean Nusselt Number

p   static pressure

Re   Reynolds number based on channel height $\dfrac{\rho\, U_{av}\, H}{\mu}$

S   surface area of a cell face

t   time

u   axial velocity

v   spanwise velocity

w   normal or vertical velocity

x   axial dimension of coordinates

y   spanwise dimension of coordinates

z   normal or vertical dimension of coordinates

T   temperature

Greek Letters

γ Upwinding Factor

α Thermal diffusivity

ρ Density of the fluid

θ Non-dimensional temperature $(T-T_\infty)/(T_w-T_\infty)$

β   angle of attack

ξ,η Coordinates in computational space

Subscripts

b   bulk condition

j   cell face

i   cell center

w   wall

Superscripts

$n,\quad n+1$ time level

Chapter 1
INTRODUCTION

1.1 Genesis of the Problem

Fin-tubes are commonly used in many gas-liquid cross-flow heat exchangers. In such an arrangement, the cooler stream (gas) generally flows across the tubes and the hot fluid (liquid / vapor) flows inside the tubes. The fins act as extended surfaces providing the bulk of the heat transfer surface area on the gas. Even with the extended surfaces, the dominant thermal resistance is on the side of the gas. In order to achieve significant heat transfer enhancement on the gas side, strategies must be developed, which will result in increased heat transfer coefficients on the fin and the tube surfaces without a large increase in pressure drop in the flow passage.

1.2 The Importance in Technology Development

Heat exchangers are widely used in power and process industries, so improvement in their performance are of great technical, economical, and ecological importance. The air-cooled condensers are generally used in geothermal power plants. Often the size of such condensers is so huge that the cost of the condenser is almost one-third of the plant cost. Accomplishment of more efficient heat transfer on the airside of the air-cooled condensers used in geothermal power plants is expected to improve the overall performance of all these plants. The reductions in size and capital cost are two other noteworthy benefits. The enhancement technique must incur modest additional pressure drop. Figure 1.1 shows a schematic diagram of the core region of fin-tube heat exchangers. While designing a compact heat exchanger, emphasis has to given to the enhancement of heat at the cost of modest increase in pressure penalty. In order to achieve this

goal, aerodynamically slender bodies may be used as protrusions on the heat transfer surfaces.

1.3   Focused area and Specific Outline of the Present Problem

The protrusions on the flat surfaces can create vortical motion that disrupts the growth of thermal boundary layer and sets a larger temperature gradient between the solid wall and the flowing fluid. The vortical motions dominated by the longitudinal vortices have remarkable influence on flow control. The longitudinal vortices can be generated by mounting delta wing or delta winglet type vortex generators on the flat surface (Figure 1.2). Biswas et al. (1994) have carried out numerical investigation on the related topic. The longitudinal vortices are developed along the side-edge of the delta-winglets due to the pressure difference between the front surface facing the flow and the back surface. The longitudinal vortices are also called the streamwise vortices since the axes of vortices are aligned to the direction of main flow. The streamwise vortices interact with an otherwise two-dimensional boundary layer and produce a three-dimensional swirling flow that mixes near wall fluid with the stream. This is a type of kinematic mixing and strongly enhances the entrainment of fluid from the periphery to the core region of the flow field. Thus the thermal boundary layer is disrupted and heat transfer is enhanced. The additional pressure drop is modest because form drag for such winglet-type slender bodies is low. Vortex generators can be mounted behind the tubes in fin-tube heat exchangers following two common configurations, – (i) common-flow-down and (ii) common-flow-up as proposed by Pauley et al. (1988).

In order to achieve the improvement of the heat exchanger surfaces, present work numerical investigation proposes use of oval tubes in place of circular tubes. In addition, delta-winglets are being proposed to be mounted in front of the oval tubes (O'Brien et al. (2001). Figure 1.3 presents a sectional view of the suggested arrangement for the finned-oval tube heat exchangers with delta-winglets placed in front of the oval tube. For such a configuration, the full Navier-Stokes

2

equations together with the energy equation have been solved. A detailed analysis of flow structure together with heat transfer characteristics provides insightful understanding of the enhancement technique.

1.3   Layout of the Thesis

In Chapter-1 we have already introduced the genesis of the problem. Chapter-2 of the thesis provides a review of the literature relevant to the understanding of the basic mechanism involved in augmentation of heat transfer and the algorithms related to solving the Navier-Stokes equations. A concise review of modeling aspect of transient flow has been focused in Chapter-2. The mathematical formulation of the problem for simulation is presented in Chapter-3. Here, the flow geometry, the governing equations, boundary conditions, grid generation, the finite volume formulation and the solution algorithm have been discussed. Chapter-4 discusses the results for laminar flow with a detailed study of flow physics and associated heat transfer. Chapter-5 includes the concluding remarks and the scope for the future research.

Liquid

Tube

Fins

Gas
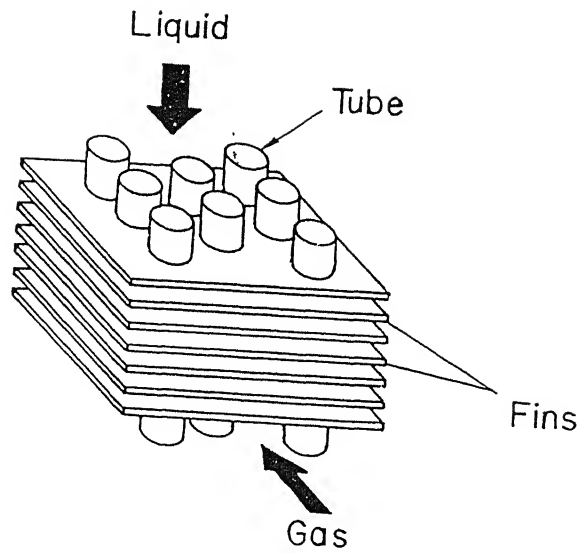
Figure 1.1   Schematic diagram of core region of a fin-tube heat exchanger

β : angle of attack

$b/_2$

l

Winglet pair
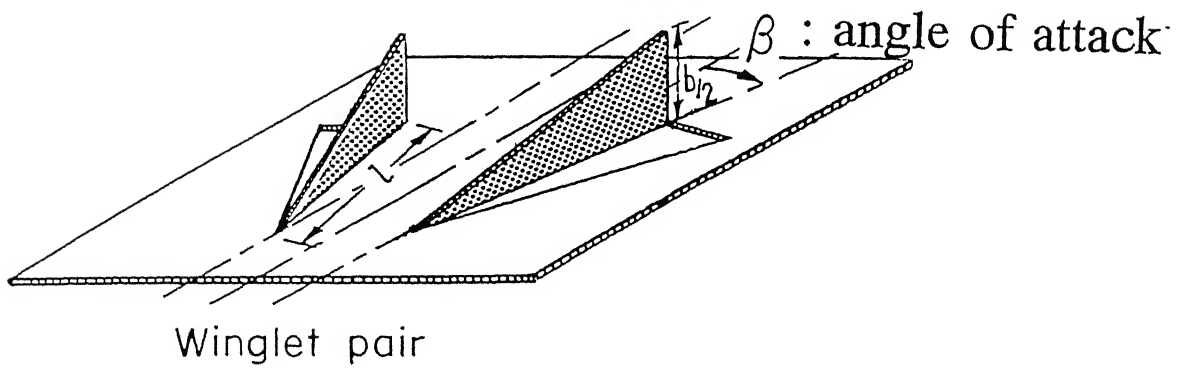
Figure 1.2   Delta-winglet type vortex generators on flat surface
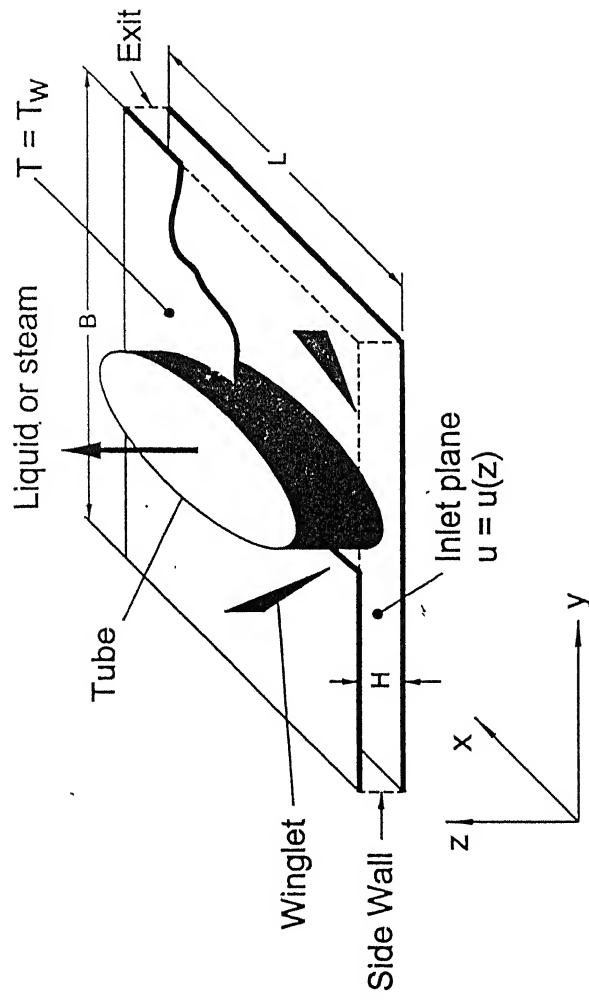
Figure 1.3   Heat Exchanger Module with an oval tube and vortex generators

Chapter 2
Literature Review

2.1 Introduction

This chapter outlines a summary of host of articles available in the areas closely related to the present investigation of enhancement of heat transfer using oval tube and winglets. The review of the articles is arranged in three different sections. In the first section, an overview of different augmentation technique is presented. The next section focuses on modeling of incompressible flows and associated heat transfer problems. The third section discusses some aspects of unsteady flow and turbulence. Finally the benefit of current problem is established from the available knowledge of the existing literature.

2.2 Augmentation of Heat transfer

Investigations on the transport enhancement using vortex generators have been carried out in the last two decades. The idea of using vortex generators in commercial heat exchangers has recently been implemented by industry. Fiebig and his co-workers (Fiebig et al., 1986) experimentally observed enhancement in heat transfer using vortex generators on the primary heat transfer surfaces. Subsequently a host of other investigations were taken up by different groups and the use of vortex generators evolved as a useful device for enhancement in heat transfer. The investigations due to Eibeck and Eaton (1987), Fiebig et al. (1989), Biswas et al. (1989), Fiebig et al. (1990), Yanagihara and Torii (1990), Fiebig et al. (1991), Biswas and Chattopadhyay (1992), Biswas et al. (1994 a), Biswas et al. (1994 b), Tigglebeck et al. (1994), Deb et al. (1995) and Valencia et al. (1996) revealed the effectiveness of using vortex generators in various types of heat exchangers. Biswas and Chattopadhyay (1992) have considered the influence of Reyonlds number and angle of attack of the delta wing type vortex generators on skin friction and Nusselt number. Although with regard to augmentation of heat

transfer in a channel, the delta wings showed better performance (Fiebig et al., 1986; Fiebig et al., 1990), it was established that the delta winglet pair is a more appropriate choice with respect to effective use of energy (Biswas et al., 1994b). The interaction of vortices with the boundary layer and its effect on heat transfer is a subject of interest to many researchers. The research topics include Taylor-Görtler vortices in boundary layers on concave surfaces; the horseshoe vortices in front of bluff objects and wingtip vortices impinging on a downstream surface. The embedded longitudinal vortex is capable of strongly perturbing the boundary layer and influencing the heat transfer characteristics. In addition, longitudinal vortices usually maintain their coherence over a long streamwise distance. As a consequence, the heat transfer effects behind the vortex generators are very persistent. Eibeck and Eaton (1987), Westphal and Mehta (1987) have worked extensively in this field with more focus to the turbulent boundary layer. Eibeck and Eaton (1987) have conducted experiments on longitudinal vortices embedded in a turbulent boundary layer and resultant heat transfer effects. An investigation on the mechanisms of heat transfer enhancement associated with the delta-wing type vortex generators has been performed by Torii et al. (1994). Biswas et al. (1996) have computed flow structure behind the winglets in a channel. They have also determined the flow structure in a similar geometrical configuration using hot wire probes. They found excellent agreement between the computational results and their experimental counterpart. Detailed local Nusselt number distributions in the first pass of a sharp turning two-pass square channel with various configurations of longitudinal vortex generator arranged on one wall have been measured by Liou et al. (2000) using unsteady liquid crystal thermography. Vasudevan et al (2000) have computed the enhancement potential of triangular fins (which are widely used inserts between the plates of the plate-fin heat exchangers) having delta winglets mounted on their slant surfaces.

2.3 Literature on incompressible flow Modeling and Associated Heat Transfer Problems

Numerical solution of full Navier-Stokes equations is performed together with the energy equation for obtaining the temperature field in any given heat transfer problem. The major difficulty in obtaining numerical solution of incompressible flows is that there is no explicit equation for pressure. The incompressible flows also exhibit spatial coupling of pressure and velocity. The pressure distribution requires justifying the condition of zero mass divergence in all computational cells. As a consequence, the pressure field cannot be solved by explicit time advancement procedure, instead it requires at least a partially implicit determination which takes into account the coupling between pressure and velocity fields as well as the effects of velocity boundary conditions. This aspect is the most distinctive feature of the primitive variable formulation of the incompressible flow modeling. To solve two-dimensional and three-dimensional problems, Harlow and Welch (1965) have used a staggered grid for the dependent variables in their well-known MAC (Marker and Cell) method. This method computes the provisional velocities by a predictor-step and the final velocity field is obtained via a corrector-step procedure. Hirt and Cook (1972) have applied a modified version of this method for the free surface flows and flow around structures and over rough terrain.

Patankar and Spalding (1972) have introduced an efficient implicit method of solving Navier –Stokes equations known as SIMPLE (Semi-Implicit Method for Pressure Linked Equations). Van Doormaal and Raithby (1984) have modified the pressure correction equation through a direct pressure-solver. This algorithm is known as SIMPLEC.

Garg and Maji (1987) have applied SIMPLEC (Van Doormaal and Raithby, 1984) method for solution of viscous flows through periodically converging-diverging tubes. In another numerical investigation, Velusamy and Garg (1993) have solved the complete set of Navier-Stokes equations for three-dimensional developing flows through elliptic cross-section ducts. Rhie and Chow (1983) and Peric (1985)

have applied the finite volume method on non-orthogonal coordinates and collocated grid arrangement. Peric et al. (1988) have shown that the collocated arrangement converges faster than the staggered variable arrangement and has advantages when extensions such as multigrid techniques and non-orthogonal grids are considered. A finite volume based procedure has successfully developed by Majumdar et al. (1992) using such collocated velocities and pressure.

2.4 Unsteady flows and Turbulence

In the experimental investigation of transport processes, Cantewell and Coles (1983) have studied the near-wake of a circular cylinder at a very high Reynolds number. Perry (1982) has demonstrated the presence of vortex shedding behind a circular cylinder at a Reynolds number of 100 with the help of a flow visualization technique. At higher Reynolds numbers, the flow becomes complex due to presence of three simultaneous instabilities, namely the boundary layer instability, separated shear layer instability and the primary vortex instability. Most of the recent developments on the flow past bluff bodies, especially the flow past a circular cylinder have been discussed elaborately in the review papers of Roshko (1993). The wake behind bluff bodies shows unsteady characteristics even at low Reynolds numbers. Reynolds number behaves as control parameter and as it is increased, detachment of the free shear layer and the consequent shedding vortices, generation of harmonics, three-dimensionality in nominally two-dimensional geometries, onset of chaos and transition to turbulence results. This by itself is a sequence of transitions, each being identified with a critical Reynolds number and an associated flow topology.

A non-linear dynamical system can go to a chaotic state through three distinct routes. These involve period doubling of frequencies (Feigenbaum, 1980), the Ruelle-Takens-Newhouse route through quasi-periodicity (Ruelle and Takens, 1971) and intermittency (Manneville and Pomeau, 1980). Vittori and Blondeaux (1983) have reported a quasi-periodic route to chaos in their numerical study of two-dimensional oscillatory flow around a circular tube. They found that the

system gets phase-locked before it becomes chaotic. In the quasi-periodic route, the dynamical system initially at a steady state becomes unsteady as the control parameter crosses a particular threshold limit. The non-linearity of the system generally increases as a result of an increase in control parameter. For example, an increase in the Reynolds number diminishes diffusion and dissipation mechanisms, resulting in greater prominence of the non-linear acceleration terms. As a consequence of instability, the dynamical behavior approaches a limit cycle caused by a Hopf bifurcation, with further increase in the control parameter, additional Hopf bifurcations take place and the system moves to the state of double frequencies. Similarly, further increase of Reynolds number leads to appearance of three frequencies. Guzman and Amon (1996) have shown a quasi-periodic and frequency locking route to chaos in two as well as three-dimensional flow through converging-diverging channels. Karniadakis and Triantafyllou (1992) have reported dynamics of a three-dimensional flow and transition to turbulence in the wake of a circular cylinder. They have found that the system undergoes a rapid transition to a chaotic three-dimensional state at a Reynolds number of 500 starting from a laminar two-dimensional state at a Reynolds number of 200.

2.5   How the Current Problem Benefits from Existing Literature

The numerical investigations of Biswas et al. (1994) and the experimental findings of Valencia et al. (1996) reveal the effective utilization of vortex generators for the purpose of enhancement of heat transfer while producing less of a pressure drop. In the above investigations, the enhancement of heat transfer from the fin surfaces is achieved by placing delta-winglet type vortex generators on the flat fin surfaces in the neighborhood of the tube. The longitudinal vortices are developed along the side-edge of the delta-winglets due to the pressure difference between the front surface facing the flow and the back surface. The longitudinal vortices are also called the streamwise vortices since the axes of vortices are aligned to the direction of main flow. The streamwise vortices

interact with an otherwise two-dimensional boundary layer and produce a three-dimensional swirling flow that mixes near wall fluid with the stream. This enhances the entrainment of fluid from the periphery to the core region of the flow field. Thus the thermal boundary layer is disrupted and heat transfer is enhanced. The additional pressure losses are modest because the form drag for such winglet-type slender bodies is low.

The air-cooled condensers of geothermal plants consist of the same fin-tube arrangement as shown in Figure 1.1. Air is forced through several rows of these fin-tubes by large fans. The condensers units can be very large, consuming a large fraction of the overall capital cost of these plants. In the present research, a three-dimensional numerical model has been formulated to provide a better understanding of the flow physics. The complete Navier-Stokes equations together with governing equations of energy are solved in an element of heat exchanger as shown in Figure 1.3. The heat exchanger element consists of a rectangular channel with a built-in oval tube and a winglet pair. A detailed analysis of the flow structure together with heat transfer characteristics in such an element is studied in this investigation. In general, the delta-winglet type vortex generators can be mounted on the flat surfaces with both common-flow-down and common-flow-up configurations. For the common-flow-down configuration, the transverse distance between the leading edges of the winglet pair is less than that of the trailing edges of the same winglet pair. While for the common-flow-up configuration, the transverse distance between the leading edges of the winglet pair is more than that of the trailing edges of the same winglet pair (Torii et al., 2000). In the present case two heat transfer strategies are being proposed to provide the improvements over the standard fin-tube heat exchangers, the first strategy involves utilization of an oval tube in place of a circular tube (Chen et al., 1998). This strategy results in a more streamlined airflow pattern around the tube and less airside pressure drop for the same flow area inside the tube. It also reduces the size of wake region downstream of the tube, which is a region of poor heat transfer. In their experimental study, O'Brien and Sohal (2000) have shown

that performance of the oval tube in such applications is indeed promising. The second strategy involves placing vortex generators on the fin surfaces in order to increase overall fin heat transfer rate by producing longitudinal vortices similar to horseshoe vortices. In this thesis, the influence of the delta winglet pair with common-flow-down and common-flow-up configurations has been studied.

Chapter 3

FORMULATION OF THE PROBLEM AND METHOD
OF SOLUTION

3.1 Introduction

The purpose of undertaking the present investigation has already been enumerated in the earlier chapters. Notwithstanding the extent of present literature on augmentation of heat transfer, a need is felt to compute three-dimensional flow in a horizontal channel with a built-in oval tube and winglet pair. This numerical simulation is capable of providing with quantitative information of flow structure, temperature distribution in the entire domain. The predictions of heat transfer to the cooler stream with its dependence on pertinent input parameters have been presented in this study.

3.2 Statement of the Problem

The two-dimensional representation of computational domain is shown in Figure 3.1. Two neighboring fins form a channel of height H, width B = 11.25 H and length L = 13.75 H. The built-in oval tube, of semi major diameter a = 4.40 H and semi minor diameter b = 1.465, is located at a distance L_1 = 6.87 H from inlet of the channel. The tube center is located at X = 6.87, Y = 5.64. Position of the winglets is shown as W1 and W2. The axial distance (X11) between the leading edge of the first winglet pair in common-flow-down configuration and the channel inlet is 1.63 H. The transverse distance (Y11) between the channel centerline and the leading edge of the winglet is 2.23 H. The axial distance (X12) between the trailing edge of the winglet and the channel inlet is 3.38 H. The transverse distance (Y12) between the channel centerline and the trailing edge of the winglet is 3.69 H. The other winglet is placed symmetrically about the channel centerline. The axial distance (X21) of the leading edge of second pair of winglets in common-flow-up configuration from the inlet of channel is 3.96 H

and transverse distance (Y21) from the centerline of the channel is 5.33 H. The axial distance (X22) between trailing edge of the second pair of winglet and channel inlet is 5.71 H and the distance (Y22) of it from the channel centerline is 3.88 H. The angle of attack for both the winglet pairs is 40^0. Length of all the winglets is 2.27 H and height is h = 0.5 H. The characteristics dimension is taken as the height of the channel. The computations are also performed for different angles of attack, such as 30^0 and 35^0. Air has been considered as the working fluid; hence Prandtl number in the present study is 0.7. Computations are performed for different Reynolds numbers, such as 500, 1000 and 1500. The winglets and oval tube are at the temperature of the channel wall.

The flow field in the channel with built-in circular tube and a winglet pair is characterized by the following parameters:

- Reynolds number
- Position of the oval tube in the channel (L_1/L)
- Velocity profile at the channel inlet
- Channel height (H/B)
- Angle of attack of the winglets (β)
- Height of the winglets (h/H)
- Position of the winglets (X_A/L, Y_A/L)

3.3   Governing Equations

The three-dimensional Navier-Stokes equations for laminar flow of an arbitrary spatial control volume V bounded by a closed surface S can be expressed in the following general convection-diffusion-source integral form

$$\frac{\partial}{\partial t}\int_V \rho \, dV \;+\; \int_S \rho\, \mathbf{u}\cdot dS \;=0 \tag{3.1}$$

$$\frac{\partial}{\partial t}\int_V \rho \phi \, dV \;+\; \int_S \left[\rho \mathbf{u}\phi - \Gamma_\phi \nabla\phi\right]\cdot dS \;=\int_V S_\phi \, dV \tag{3.2}$$

14

where ρ represents the fluid density, $\mathbf{u}$ is the fluid velocity, ϕ stands for any vector component or scalar quantity, S_ϕ is the volumetric source term. For incompressible flow of Newtonian fluid, the equation takes the form

$$\int_S \mathbf{u}.dS = 0 \qquad (3.3)$$

$$\frac{\partial}{\partial t}\int_V \rho\phi\, dV \quad + \quad \int_S [\rho\mathbf{u}\phi - \Gamma_\phi \nabla\phi].dS = \int_V S_\phi dV \qquad (3.4)$$

and the source term for momentum equation becomes $-\frac{1}{\rho}\int_S p\,I.dS$ where I is the unit tensor. In this formulation we work with Cartesian components of velocity. So ϕ can be the three-Cartesian components of velocity u, v, w as well as any scalar e.g., temperature which need to be determined. The variables of the general transport equation are given in Table-3.1.

Table 3.1

Equation	ϕ	Γ_ϕ	S_ϕ
Continuity	1	0	0
Momentum	U_j	μ	$\dfrac{\partial p}{\partial x_j}$
Energy	T	$\dfrac{k}{C_P}$	0

3.4 Boundary Conditions

The governing differential equations are elliptic in space and parabolic in time. We need the boundary conditions for all the confining surfaces. The boundary conditions of interest in the present investigation are:

- Top and bottom plates

$u=v=w=0,$ (No Slip boundary condition) and $\dfrac{\partial p}{\partial z} = 0$

15

$$T = T_w \qquad (T_w \text{ represents wall temperature})$$

- Side Wall

$$\frac{\partial u}{\partial y} = \frac{\partial w}{\partial y} = 0, \quad v = 0 \qquad \text{(Free Slip boundary condition) and } \frac{\partial p}{\partial y} = 0$$

$$\frac{\partial T}{\partial y} = 0$$

- Channel Inlet

$$u = u_\infty, \quad v = w = 0, \qquad \text{and} \quad \frac{\partial p}{\partial x} = 0$$

$$T = T_\infty$$

- Channel Exit

The mass flux through the outlet boundaries is found by means of a continuative outflow condition (Orlanski, 1976), which allows changes inside the flow field to be transmitted outward, but not vice-versa.

$$\frac{\partial \phi}{\partial t} + U_{av.} \frac{\partial \phi}{\partial x} = 0 \qquad \text{(Where } \phi \text{ represents u, v, w or T)}$$

$$p = p_\infty$$

Obstacles: Oval tube and the Winglet pair

$$u = v = w = 0, \text{ and } \frac{\partial p}{\partial n} = 0 \qquad \text{(where n signifies normal direction)}$$

and $T = T_w$

3.5   Grid Generation

Figure 3.2 shows the two-dimensional grid for the computational domain. BLOCK PARTIONING is being used to generate the grid. The whole computational domain is divided into two blocks. In one block, Cartesian grid is generated, where winglets are mounted on the fin-surface; while in other block oval tube is placed. A differential equation is used to generate the body fitting type grid where oval tube exists. The two dimensional grid is stacked layer by a

16

layer with constant value in third direction to generate the grid in that direction. Initially two-dimensional grid is generated by the transfinite interpolation, which uses essentially linear interpolation scheme to compute the interior points by using the points from the computational domain boundaries. Thus it results an algebraic grid, which is further smoothened by the use of Partial Differential Equations (PDE). In this technique, a system of elliptical PDEs is solved for obtaining the location of grid points in the physical space, whereas the computational grid is rectangular shape uniformly spaced. A Laplace equation or a Poisson equation with a Dirchlet boundary condition can be used for this purpose. Here we use Laplace equation as

$$\nabla^2 \xi = 0 \tag{3.5}$$

$$\nabla^2 \eta = 0 \tag{3.6}$$

To get the location of interior points from the boundary, the above equation is solved by finite difference technique. The initial guess that is needed to solve the Laplace equation is taken from the algebraic mapping. This operator can provide quite smooth grids. Due to curvature of the boundary, it has been observed that there is concentration of grid lines, which can be solved by the using the appropriate control functions in the Poisson Equation, but the use of control functions added more complexity in the transformed domain.

3.6   Computational Procedure for Grid Generation

The algorithm used for the generation of the present grid can be outlined as follows:

1. Geometrical data is used as input.
2. On the basis of number of grid points, the computational grid is defined (on ξ, η).
3. Now the boundary points along the edges of the physical domain are defined.
4. Algebraic grid is used to generate the initial guess, which is used by the Laplacian operator. Following linear interpolation technique is used to compute at any interior points

$$X'_P = (1 - \xi) X_E + \xi X_F \tag{3.7a}$$

$$Y'_P = (1 - \eta) Y_E + \eta Y_F \tag{3.7b}$$

where E and F are the two boundary grid points.

5. Using four-point formula, guess is further improved a little.

6. Elliptical grid generation system constitute of following equations derived from the Laplace operator.

$$\alpha x_{\xi\xi} - 2\beta x_{\xi\eta} + \lambda x_{\eta\eta} = 0 \tag{3.8}$$

$$\alpha y_{\xi\xi} - 2\beta y_{\xi\eta} + \lambda y_{\eta\eta} = 0 \tag{3.9}$$

where

$$\alpha = x_\eta^2 + y_\eta^2 \tag{3.10}$$

$$\beta = x_\xi x_\eta + y_\xi y_\eta \tag{3.11}$$

$$\lambda = x_\xi^2 + y_\xi^2 \tag{3.12}$$

These coefficients are determined using finite difference approximations. The x and y values in these expressions are provided by the initial distributions for the first iteration, and subsequently from the previous iteration, i.e., the computation of coefficients lag by one iteration level. The iterative solution continues until a specified convergence criterion is met.

The truncation error in numerical analysis is much dependent on the nature of gird, because of finite difference approximations. We target for such a grid, which gives minimum truncation error. The following parameters affect the quality of the grid:

1. Transformation Jacobean
2. Skewness
3. Aspect Ratio
4. Adjacent cell ratio

All the parameters were calculated and their values were well within the acceptable limit.

3.7 Finite Volume Method

The finite-volume method (Eswaran et al., 1998) has been used to discretize the governing conservations equations. The solution domain is divided into finite

control volume whose vertices are connected by straight lines. Grid generation is used to compute the coordinates of vertices of the control volume. In this method, a collocated grid arrangement is used, in which all the dependent variables such as u, v, w, p, and T are defined at the center of the control volume (Figure 3.3). E, W, N, S, T and B are the six adjacent control volumes for the east, west, north, south, top and bottom neighbors. The face center points i.e. point of intersection of the mid points of opposite edges are denoted by small letters e, w, n, s, t and b. For example, te denotes the mid-point of the edge that contains the top face (t) and east face (e) and similarly for others. The advantages of the collocated grid over staggered grids, especially when the non-orthogonal coordinates are:

- There is only one set of control volume as all the variables share the same location.

- The convection contribution to the coefficients in the discretized equations is same for all variables.

- When coordinate oriented velocity components are used, it results in simpler equations.

- Number of constraints on the numerical grid is reduced.

3.8 Surfaces areas and Volumes

Figure 3.3 shows the corners points of the control volume numbered as 1,2,3, etc. The outward surface normal and volume can be found in the following manner as suggested by Kordulla and Vinkur (1983).

Defining $\mathbf{r}_{ij} = \mathbf{r}_i - \mathbf{r}_j$ where $\mathbf{r}_i$ and $\mathbf{r}_j$ indicate the position vectors of points i and j respectively, we have the formulae for calculating the surface area and volume for different faces.

- East Face $\qquad \mathbf{S}_e = \dfrac{1}{2}\,(\mathbf{r}_{74} \times \mathbf{r}_{83})$ $\qquad$ (3.13)

- West Face $\qquad \mathbf{S}_w = \dfrac{1}{2}\,(\mathbf{r}_{16} \times \mathbf{r}_{52})$ $\qquad$ (3.14)

- North Face $\qquad S_n = \dfrac{1}{2}(\mathbf{r}_{27} \times \mathbf{r}_{63})$ $\hfill (3.15)$

- South Face $\qquad S_s = \dfrac{1}{2}(\mathbf{r}_{18} \times \mathbf{r}_{45})$ $\hfill (3.16)$

- Top face $\qquad S_t = \dfrac{1}{2}(\mathbf{r}_{75} \times \mathbf{r}_{68})$ $\hfill (3.17)$

- Bottom Face $\qquad S_b = \dfrac{1}{2}(\mathbf{r}_{13} \times \mathbf{r}_{24})$ $\hfill (3.18)$

The volume of the cell is calculated from the cell coordinates, with the assumption that the linear segments to form the six cell faces join the cell corners. The volume is calculated as follows:

$$V = \frac{1}{3}\,\mathbf{r}_{71} \cdot (S_s + S_b + S_w) \qquad (3.19)$$

3.9 Discretization Procedure

The main steps for the discretization of the integral governing equations involve the calculation of convection and the diffusion fluxes and source terms. The rates of change and source terms are integrated over the cell volume, whereas the convection and the diffusion terms form the sum of fluxes through the faces of the control volume.

3.9.1 Discretization of Continuity Equation

Equation 3.1 is discretized in the following manner:

$$\int_S \rho u \cdot dS \approx \sum_{j=e,w,n,s,t,b} \rho(u \cdot S)_j = \sum_j \rho u_j \cdot S_j \qquad (3.20)$$

Where S_j is the surface vector representing the area of the jth cell face and u_j is the velocity defined at the face center j.

Thus it results in the following form of continuity equation

$$\sum_j F_j = F_e + F_w + F_n + F_s + F_t + F_b = 0 \qquad (3.21)$$

where the F_j is the outward mass-flux through face j, defined by:

$$F_j = \rho \, u_j \cdot S_j$$

3.9.2 Discretization of General Equation

Rate of Change

The value of dependent variable ϕ at the centroid of the control volume represents an average over the CV as a whole. Thus

$$\frac{\partial}{\partial t} \int_V \rho \phi \, dV \approx \frac{(\rho \phi V)_P^{n+1} - (\rho \phi V)_P^n}{\Delta t} \approx \rho V \frac{\phi_P^{n+1} - \phi_P^n}{\Delta t} \qquad (3.22)$$

Where V is the volume of the cell.

Convection Fluxes

The surface integral over convection flux of variable ϕ can be approximated in the following form

$$\int_S \rho u \phi \cdot dS \approx \sum_j \rho \phi_j (u \cdot S)_j = \sum_j F_j \phi_j \qquad (3.23)$$

Where ϕ_j is the value of ϕ at the center of face j. Thus

$$\int_S \rho u \phi \cdot dS \approx F_e \phi_e + F_w \phi_w + F_n \phi_n + F_s \phi_s + F_t \phi_t + F_b \phi_b \qquad (3.24)$$

Where, ϕ_e is the (interpolated) value of the variable ϕ at the east face center, etc. This can be evaluated by using a central difference linear interpolation between the neighboring nodal values ϕ_P and ϕ_E. At east face the value of ϕ_e is given by

$$\phi_e = \frac{V_E}{V_E + V_P} \phi_P + \frac{V_P}{V_E + V_P} \phi_E \qquad (3.25)$$

Where V_E and V_P are volumes of the cells around the points E and P respectively and ϕ_E and ϕ_P are the values of the dependent variables at these points. In a collocated grid system, all dependent variables are defined at the same location hence exactly the same interpolation scheme is used to express all of them at the interfaces. The central difference approximation to compute the convection flux may lead to numerical stability therefore it is blended with fist order upwind differencing scheme (UDS) as follows

$$F_e \phi_e = (F_e \phi_e)^{CDS} + \gamma ((F_e \phi_e)^{UDS} - (F_e \phi_e)^{CDS}) \qquad (3.26)$$

The upwind differencing scheme is based on assumption that the convected flux at cell face is equal to that at upstream cell along the same coordinate direction. Thus the value ϕ_e at east face is assigned the value ϕ_P if $u_e \geq 0$. This can be conveniently summarized as

$$F_e \phi_e \; = \; F_e(\frac{V_E}{V_E + V_P} \phi_P + \frac{V_P}{V_E + V_P} \phi_E) \; + \; \gamma \{ \; \phi_P [[F_e, 0]] \; - \phi_E [[-F_e, 0]] -$$

$$F_e (\frac{V_E}{V_E + V_P} \phi_P + \frac{V_P}{V_E + V_P} \phi_E) \; \} \qquad (3.27)$$

$$F_w \phi_w \; = \; F_w(\frac{V_W}{V_W + V_P} \phi_P + \frac{V_P}{V_W + V_P} \phi_W) \; + \; \gamma \{ \; \phi_P [[F_w, 0]] - \phi_W [[-F_w, 0]] \; -$$

$$F_w (\frac{V_W}{V_W + V_P} \phi_P + \frac{V_P}{V_W + V_P} \phi_W) \; \} \qquad (3.28)$$

$$F_n \phi_n \; = \; F_n(\frac{V_N}{V_N + V_P} \phi_P + \frac{V_P}{V_N + V_P} \phi_N) \; + \; \gamma \{ \; \phi_P [[F_n, 0]] - \phi_N [[-F_n, 0]] -$$

$$F_n (\frac{V_N}{V_N + V_P} \phi_P + \frac{V_P}{V_N + V_P} \phi_N) \; \} \qquad (3.29)$$

$$F_s \phi_s = F_s \left(\frac{V_S}{V_S + V_P} \phi_P + \frac{V_P}{V_S + V_P} \phi_S \right) + \gamma \{ \phi_P [[F_s, 0]] - \phi_S [[-F_s, 0]] -$$

$$F_s \left(\frac{V_S}{V_S + V_P} \phi_P + \frac{V_P}{V_S + V_P} \phi_S \right) \} \tag{3.30}$$

$$F_t \phi_t = F_t \left(\frac{V_T}{V_T + V_P} \phi_P + \frac{V_P}{V_T + V_P} \phi_T \right) + \gamma \{ \phi_P [[F_t, 0]] - \phi_T [[-F_t, 0]] -$$

$$F_t \left(\frac{V_T}{V_T + V_P} \phi_P + \frac{V_P}{V_T + V_P} \phi_T \right) \} \tag{3.31}$$

$$F_b \phi_b = F_t \left(\frac{V_B}{V_B + V_P} \phi_P + \frac{V_P}{V_B + V_P} \phi_B \right) + \gamma \{ \phi_P [[F_b, 0]] - \phi_B [[-F_b, 0]] -$$

$$F_b \left(\frac{V_B}{V_B + V_P} \phi_P + \frac{V_P}{V_B + V_P} \phi_B \right) \} \tag{3.32}$$

The symbol $[[,]]$ signifies greatest of the two quantities inside the brackets and γ is upwind factor.

In a fully implicit method the upwind parts of the above equations are implicit and they are incorporated in the coefficients of the unknown velocity during the pressure-velocity iterations. The CDS terms on the other hand are evaluated using the previous iteration values and used as a source term on the right side of the same equation. This is the so-called deferred correction approach of Khosla and Rubin (1974). Multiplication of the explicit part by a factor of γ ($0 \leq \gamma \leq 1$) allows the introduction of numerical diffusion. For the first order upwind difference scheme, $\gamma = 1$ and for the second order central difference, $\gamma = 0$. The deferred correction approach enhances the diagonal dominance of the coefficient matrix. However, the present solution scheme being explicit, the accuracy depends on the value of γ.

Diffusion Fluxes

Diffusion fluxes for the finite volume were calculated first time by Peric(1985). Later Ferziger and Peric (1999) and Eswaran and Prakash (1998) have also explained the means of expressing diffusion fluxes on different faces of arbitrary shaped differential CVs. The entire procedure has been explained in a recent work Prabhakar et al. (2001). Diffusion flux of a variable ϕ through the cell faces in the following manner

$$\int_S \Gamma_\phi \nabla\phi \cdot dS \approx \sum_{j=e,w,n,s,t,b} \left(\Gamma_\phi \nabla\phi \cdot S\right)_j = \sum_j -F_j^d \tag{3.33}$$

For any face, Surface vector can be expressed as

$$S_j = \alpha_1 n^1 + \alpha_2 n^2 + \alpha_3 n^3 \tag{3.34}$$

Where n^1, n^2 and n^3 are any three linearly independent (not necessarily orthogonal) unit vectors. Therefore

$$\begin{aligned} \nabla\phi \cdot S_j &= \nabla\phi \cdot \left(\alpha_1 n^1 + \alpha_2 n^2 + \alpha_3 n^3\right) \\ &= \alpha_1 \nabla\phi \cdot n^1 + \alpha_2 \nabla\phi \cdot n^2 + \alpha_3 \nabla\phi \cdot n^3 \end{aligned} \tag{3.35}$$

If $\Delta\phi^1, \Delta\phi^2, \Delta\phi^3$ are the differences in ϕ between the two ends of the line segments $\Delta x^1, \Delta x^2, \Delta x^3$, then

$$\Delta\phi^1 = \nabla\phi \cdot \Delta x^1, \quad \Delta\phi^2 = \nabla\phi \cdot \Delta x^2, \quad \Delta\phi^3 = \nabla\phi \cdot \Delta x^3 \tag{3.36}$$

If $\Delta x^1, \Delta x^2, \Delta x^3$ are in the directions of n^1, n^2 and n^3 respectively, then it follows from equation (3.36) that

$$\frac{\Delta\phi^1}{\Delta x^1} = \nabla\phi \cdot n^1, \quad \frac{\Delta\phi^2}{\Delta x^2} = \nabla\phi \cdot n^2, \quad \frac{\Delta\phi^3}{\Delta x^3} = \nabla\phi \cdot n^3 \tag{3.37}$$

Where Δx^1, Δx^2 and Δx^3 are the magnitudes of Δx^1, Δx^2 and Δx^3. Combining equations (3.35) and (3.37) we have

$$\nabla \phi \cdot S = \quad \alpha_1 \frac{\Delta \phi^1}{\Delta x^1} + \alpha_2 \frac{\Delta \phi^2}{\Delta x^2} + \alpha_3 \frac{\Delta \phi^3}{\Delta x^3} \tag{3.38}$$

To obtain α_1, α_2 *and* α_3, we express

$$\begin{aligned}
\mathrm{n}^1 &= \begin{pmatrix} n_{11} & n_{12} & n_{13} \end{pmatrix} \\
\mathrm{n}^2 &= \begin{pmatrix} n_{21} & n_{22} & n_{23} \end{pmatrix} \\
\mathrm{n}^3 &= \begin{pmatrix} n_{31} & n_{32} & n_{33} \end{pmatrix}
\end{aligned} \tag{3.39}$$

Where n_{11}, n_{12}, n_{13} are the Cartesian components of **n** and which can be easily

determined by $\dfrac{\Delta \mathrm{x}_1^1}{\Delta x^1}$, $\dfrac{\Delta \mathrm{x}_2^1}{\Delta x^2}$, $\dfrac{\Delta \mathrm{x}_3^1}{\Delta x^3}$, where Δx_1^1, Δx_2^1, Δx_3^1 are the three components

of vector $\Delta \ \mathrm{x}^1$, etc. The other values $n_{21} \ldots n_{33}$ can be similarly obtained. Hence equation (3.34) can be written as

$$\begin{bmatrix} n_{11} & n_{12} & n_{13} \\ n_{21} & n_{22} & n_{23} \\ n_{31} & n_{32} & n_{33} \end{bmatrix}^T \begin{bmatrix} \alpha_1 \\ \alpha_2 \\ \alpha_3 \end{bmatrix} = \begin{bmatrix} S_{1j} \\ S_{2j} \\ S_{3j} \end{bmatrix} \tag{3.40}$$

Where S_{1j}, S_{2j}, S_{3j} are the Cartesian components of the surface vector S_j

Using Cramer's rule

$$\alpha_1 = \frac{D_1}{D}, \quad \alpha_2 = \frac{D_2}{D}, \quad \alpha_3 = \frac{D_3}{D} \tag{3.41}$$

Where D is the determinant of the coefficient matrix. D_1 is obtained by replacing

the first column of D by the column with the elements S_{1j}, S_{2j}, and S_{3j}. Thus

α_1, α_2, and α_3 are determined.

The diffusion flux consists of two parts: normal derivative diffusion flux and cross derivative diffusion flux. The normal derivative flux of any dependent variable ϕ through any cell face involves the values of ϕ at cell centers whereas the cross-derivative diffusion flux involves the value of ϕ at the edge center values. The normal derivative flux is treated implicitly and is coupled with the implicit part of the convective flux to calculate the main coefficients of the discretized equations. The cross-derivative diffusion flux is treated explicitly to avoid the possibility of producing negative coefficients in an implicit treatment. This term together with explicit part of convective flux is added to the source term. The example of the east face is taken to illustrate the diffusion model (Figure-3.4). Given the edge center values ϕ_{te}, ϕ_{be}, ϕ_{se}, ϕ_{ne} we can get the normal

diffusion term $\dfrac{\phi_E - \phi_P}{\Delta x^1}$, and the cross diffusion term $\dfrac{\phi_{te} - \phi_{be}}{\Delta x^2}$ and $\dfrac{\phi_{se} - \phi_{ne}}{\Delta x^3}$.

Finally, the diffusion flux is computed by

$$F_j^d = -\Gamma_\phi\left(\alpha_1 \frac{\phi_E - \phi_P}{\Delta x^1} + \alpha_2 \frac{\phi_{te} - \phi_{be}}{\Delta x^2} + \alpha_3 \frac{\phi_{ne} - \phi_{se}}{\Delta x^3}\right) \tag{3.42}$$

For the evaluation of cross-derivative flux, the following interpolation scheme is used to obtain the edge center values

$$\phi_{te} = \frac{V_{TE}}{V_{tot}}\phi_P + \frac{V_P}{V_{tot}}\phi_{TE} + \frac{V_T}{V_{tot}}\phi_E + \frac{V_E}{V_{tot}}\phi_T \tag{3.43}$$

$$V_{tot} = V_{TE} + V_P + V_T + V_E$$

$$\phi_{be} = \frac{V_{BE}}{V_{tot}}\phi_P + \frac{V_P}{V_{tot}}\phi_{BE} + \frac{V_B}{V_{tot}}\phi_E + \frac{V_E}{V_{tot}}\phi_B \tag{3.44}$$

$$V_{tot} = V_{BE} + V_P + V_B + V_E$$

$$\phi_{ne} = \frac{V_{NE}}{V_{tot}}\phi_P + \frac{V_P}{V_{tot}}\phi_{NE} + \frac{V_N}{V_{tot}}\phi_E + \frac{V_E}{V_{tot}}\phi_N \tag{3.45}$$

$$V_{tot} = V_{NE} + V_P + V_N + V_E$$

$$\phi_{se} = \frac{V_{SE}}{V_{tot}}\phi_P + \frac{V_P}{V_{tot}}\phi_{SE} + \frac{V_S}{V_{tot}}\phi_E + \frac{V_E}{V_{tot}}\phi_S \tag{3.46}$$

$$V_{tot} = V_{SE} + V_P + V_S + V_E$$

Where, V_{TE} is the volume of the cell that is located at the top-east of the cell P. The other edge center values of the dependent variables can be interpolated in the same way.

SOURCES

The source term, which is integrated over the control volume, in the discretized equation can be considered as

$$\int_V S_\phi dV \approx \left(S_\phi\right)_P V \tag{3.47}$$

Apart from the real source S_ϕ, explicitly treated parts of the convection and diffusion fluxes may be added to S_ϕ. The pressure term in the momentum equations is also treated explicitly. Its discretization is analogous to that of the ordinary diffusion flux, i.e. for the ith momentum equation the pressure term is

$$-\int_S p \mathbf{n}_i \cdot S \quad \approx \quad \sum_j p_j S_{ij} \tag{3.48}$$

Where p_j is the pressure at the jth face center and S_{ij} is the Ith component of the surface vector for space j.

3.10 Pressure-Velocity Coupling

Simplified Marker and Cell (SMAC) method is used to obtain the velocity and pressure field that satisfies the mass and momentum equation. It is a semi-explicit method and it provides an efficient and easy way of pressure velocity coupling. The momentum equations are discretized in an explicit manner while the pressure gradient terms are treated implicitly, and the continuity equations are also enforced implicitly. Momentum and continuity equations can be expressed as

$$\rho V \frac{u_P^{n+1} - u_P^n}{\Delta t} + \sum_j \left(F^c + F^d\right)^n = -\sum_j p_j^{n+1} S_{ij} \tag{3.49}$$

and

$$\sum_j F_j^{n+1} = 0 \qquad (3.50)$$

The momentum equations are solved using the guess values of velocity and pressure field. The provisional velocity components u_i^* are calculated from the following equation

$$u_P^* = u_P^\circ - \frac{\Delta t}{\rho V_P}\left(F_P^c + F_P^d\right) + \frac{\Delta t}{\rho V_P} S_u \qquad (3.51)$$

Where u_P° is the value of velocity at earlier iteration and S_u is the pressure term. This provisional velocity in general will not satisfy the continuity equation. The continuity equation (3.50) in another form reads as follows:

$$\sum_j \left(F_j^* + F_j'\right) = 0$$

$$\sum_j F_j' = -\sum_j F_j^* \qquad (3.52)$$

where F_j^* is the uncorrected mass flux obtained from the provisional velocities and F_j' is the mass flux correction. To evaluate the terms on the right side of equation (3.52), it is necessary that the variables (velocities and pressure) are to be known at the cell faces. Due to the non-staggered arrangement, if the variables at the cell faces are evaluated by linear interpolation between the adjacent cell center quantities then the pressure iteration does not converge. The solution leads to a Checker Board pressure field (i.e., spurious oscillation of pressure may occur), as shown by Rhie (1981). Majumdar (1988) has explained the concept of Momentum Interpolation to circumvent this problem. The essence of the concept is that the velocities at the cell faces are computed by linear interpolation of the convective and diffusive terms but not the pressure term. Thus the method with the collocated variable arrangement relies indirectly on the staggering idea. Following this idea the interpolated velocity at the east face of the control volume given by is obtained in the following manner

$$u_e = \overline{\left(v_P, v_E\right)} - \frac{\Delta t}{\rho}\nabla p \qquad (3.53)$$

where

$$v_P = u_P^\circ - \frac{\Delta t}{\rho V_P}\left(F_P^c + F_P^d\right) \qquad (3.54)$$

$$v_E = u_E^\circ - \frac{\Delta t}{\rho V_E}\left(F_E^c + F_E^d\right) \qquad (3.55)$$

And the over bar indicates a linear interpolation using equation (3.25). So the uncorrected mass flux for the east face using equation (3.53) becomes

$$F_e^* = \rho u_e \cdot S_e = \rho \overline{\left(v_P, v_E\right)} \cdot S_e - \Delta t \nabla p \cdot S_e \qquad (3.56)$$

Equation (3.56) in its generalized form for any cell face is in the form

$$F_j^* = \rho v_j \cdot S_j - \Delta t \nabla p_j \cdot S_j \qquad (3.57)$$

To enforce mass conservation, the velocity and pressure corrections are introduced, linked by

$$u_j' = -\frac{\Delta t}{\rho} \nabla p_j' \qquad (3.58)$$

This step simulates the effect of a staggered grid (face-center velocity and cell-center pressure) and reaps the benefits of faster convergence. From equation (3.58) we get the mass flux correction at the face j

$$F_j' = \rho u_j' \cdot S_j = -\Delta t \nabla p_j' \cdot S_j' \qquad (3.59)$$

Since equation (3.59) is exactly of the same form as equation for diffusion flux equation (3.33), with only the variables interchanged, therefore the same method can be used for computing F_j'

Combining equations (3.52), (3.57) and (3.59) yields

$$-\Delta t \nabla p_j' \cdot S_j = \rho V_j \cdot S_j - \Delta t \nabla p_j \cdot S_j$$

Or $\qquad\qquad \Delta t \nabla p_j' \cdot S_j + S_m = 0 \qquad (3.60)$

$$\left(S_m = \rho V_j \cdot S_j - \Delta t \nabla p_j \cdot S_j\right)$$

Which gives the *pressure* correction equation. After the solution of the pressure correction equation, the nodal velocity, mass fluxes and pressure are updated. The corrected pressure p^{n+1} is obtained by

$$p^{n+1} = p^n + p'$$

(3.61)

$$u'_P = -\frac{\Delta t}{\rho V_P} \sum_j p'_j S_{ij}$$

(3.62)

$$u_i^{n+1} = u_i^* + u_i'$$

(3.63)

The energy equation is discretized and solved by using this new velocity distribution. On integrating the conservative form of the steady state energy equation over a control volume, neglecting the dissipative terms, as it is significant for high speed flows, the temperature equations becomes

$$\alpha \sum_j (\nabla T \cdot S)_j = \sum_J \rho u \cdot \cdot S_J)T_j$$

(3.64)

which is solved by SOR method to get the temperature distribution at the current time step.

The first terms of equation (3.60) and equation (3.64) are expanded following the philosophy that was followed during the discretization of equation (3.23). Subsequent regrouping of the normal derivative terms yields the standard *Poisson Equation*. The Poisson equation can be solved by a multitude of methods. We have used the Gauss-Siedel iterative method, which is quite reliable and robust. The flow chart with the main steps of the algorithm is given in Figure 3.5.

3.11 Solution Algorithm

The velocity pressure and temperature fields are calculated by the following the procedure of Eswaran and Prakash (1998). The procedure can be summarized in the following way:

1. Make initial guess of the pressure, velocity and temperature fields. Use equations (3.51) and (3.54) to calculate cell center u_P and v_P. Use linear interpolation equation (3.25) to obtain the face center quantities VJ.

2. Compute the mass flux through cell face j using equation (3.57).

30

3. Use equation (3.58) to compute the flux correction at the cell face j using equation (3.59), which is computed using the formulation for diffusion fluxes i.e. equations (3.33) to (3.46). For calculating by F_j', the variable ϕ is to be replaced by p'.

4. Compute the residue, $\Re$ for each cell

$$\Re = -\sum_j F_j^* - \sum_j F_j'$$

5. Calculate the cell-center pressure correction (using Gauss-Siedel method) from the relation

$$p_P' = p_P' + \omega \frac{\Re}{a_P \Delta t}$$

where ω is the relaxation factor and a_P stands for the diagonal coefficients of equation (3.60), which is calculated from

$$a_P = -\left[\frac{\alpha_1}{\Delta x^1}\bigg|_w - \frac{\alpha_1}{\Delta x^1}\bigg|_e + \frac{\alpha_2}{\Delta x^2}\bigg|_n - \frac{\alpha_2}{\Delta x^2}\bigg|_s + \frac{\alpha_3}{\Delta x^3}\bigg|_s - \frac{\alpha_3}{\Delta x^3}\bigg|_t \right]$$

where α_1, α_2 etc are the same as that are used in equation (3.33) to (3.46).

6. If $\Re_{rms} > \varepsilon$ go to step 3.

7. Store the updated mass flux through cell faces using equation (3.57).

8. Store the updated pressure at the center of the cells

$$p_P = p_P + p_P'$$

9. Store the cell-center corrected velocity

$$u_P' = -\frac{\Delta t}{\rho V_P} \sum_j p_j' S_{ij}$$

$$u_i^{n+1} = u_i^* + u_i'$$

10. Calculate the residual for each cell

$$\tilde{\Re} = \alpha \sum_j (\nabla T \cdot S)_j = \sum_j \rho u \cdot S_j)T_j$$

11. Calculate the cell-center temperature using Gauss-Seidel method to obtain

$$T_P = T_P + \Omega \frac{\tilde{\Re}}{b_P \alpha}$$

Where Ω is the relaxation factor and b_P stand for the diagonal coefficients of equation (3.64) i.e., calculated from the relation

$$b_P = - a_P$$

12. If $\tilde{\mathfrak{R}}_{rms} > \varepsilon$ go to step 10.

13. Go to step 1 and repeat the process until the steady state is reached.

It can be shown that solving equation (3.52) is same as solving

$$\nabla^2 p' = -\rho \frac{\nabla \cdot u_j^*}{\Delta t}$$

and finding the corrections

$$u_j' = -\frac{\nabla t}{\rho} \nabla p'$$

such that

$$u_i^{n+1} = u_i^* + u_i'$$

$$p^{n+1} = p^n + p'$$

Thus the procedure above can be called solution of **Pressure Linked Equations**.

3.12 Numerical Stability Considerations

Time step impose certain restrictions on Semi-Explicit method, which relies on explicit differences. For a given mesh the choice of time step is determined through stability analysis, which has to take care two conditions. First, fluid should not be allowed to cross more than one cell in any one-time step. This restrictions is derived from the Courant-Friedrichs-Lewy (CFL) conditions given by

$$\delta t_1 < \min \left\{ \frac{\delta x}{|u|}, \frac{\delta y}{|v|}, \frac{\delta z}{|w|} \right\} \tag{3.65}$$

Where the minimum is with respect to every cell in the domain. Typically δt_1 is chosen equal to one-third to two-third of the minimum cell transient time.

Secondly, when a non-zero value of kinematic viscosity is used momentum must not diffuse more than approximately one cell in one time step. A linear stability analysis shows that the restrictions on grid Fourier number will yield

$$\delta t_2 < \frac{1}{2} \frac{(\delta x)^2 (\delta y)_2 (\delta z)^2}{(\delta x)^2 + (\delta y)^2 + (\delta z)^2} Re \qquad (3.66)$$

Finally, the minimum of the two above time increments is chosen for computation.

L=13.75 H
B=11.25 H
X11=1.63 H
X12=3.38 H
Y11=2.23 H
Y12=3.69H
X21=3.96 H
X22=5.71 H
Y21=5.33 H
Y22=3.88 H
l=2.27 H
h=0.5 H
a=4.40 H
b=1.465 H
L_1=6.87 H
β = 40°

COMMON-FLOW-UP

COMMON-FLOW-DOWN
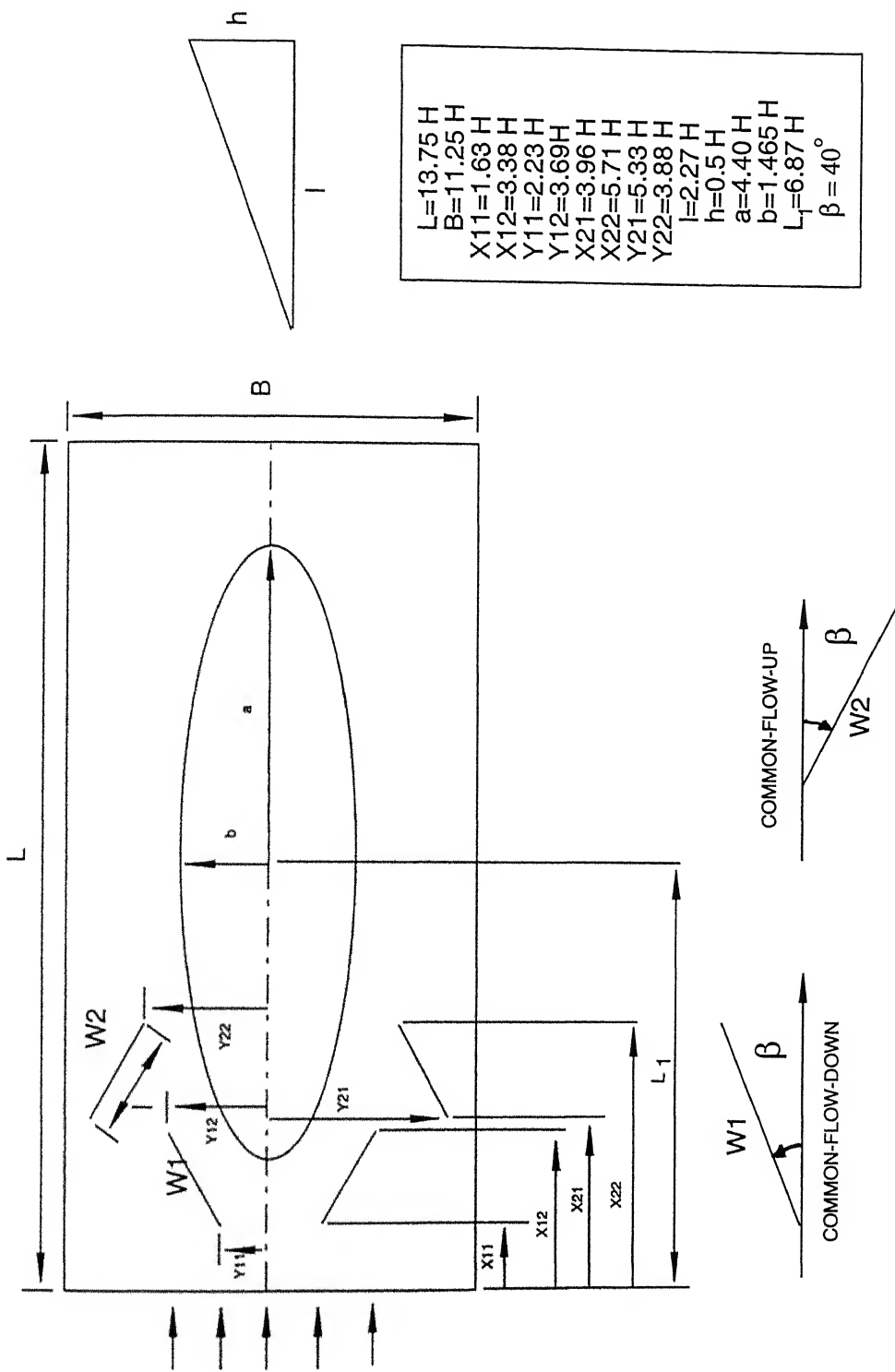
Figure 3.1   Two-Dimensional representations of Computational Domain

OVAL TUBE

Figure 3.2   The Two Dimensional Grid for the
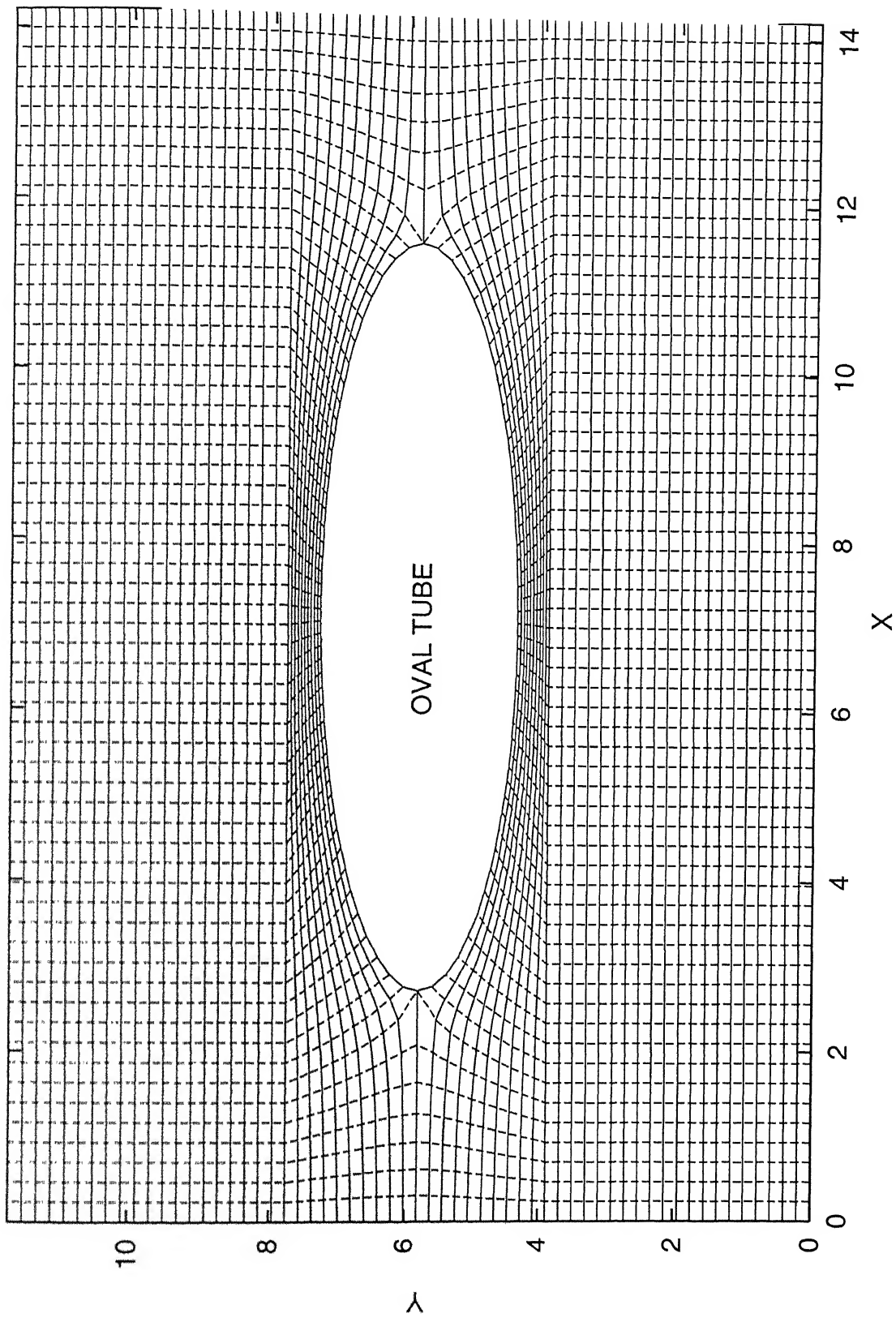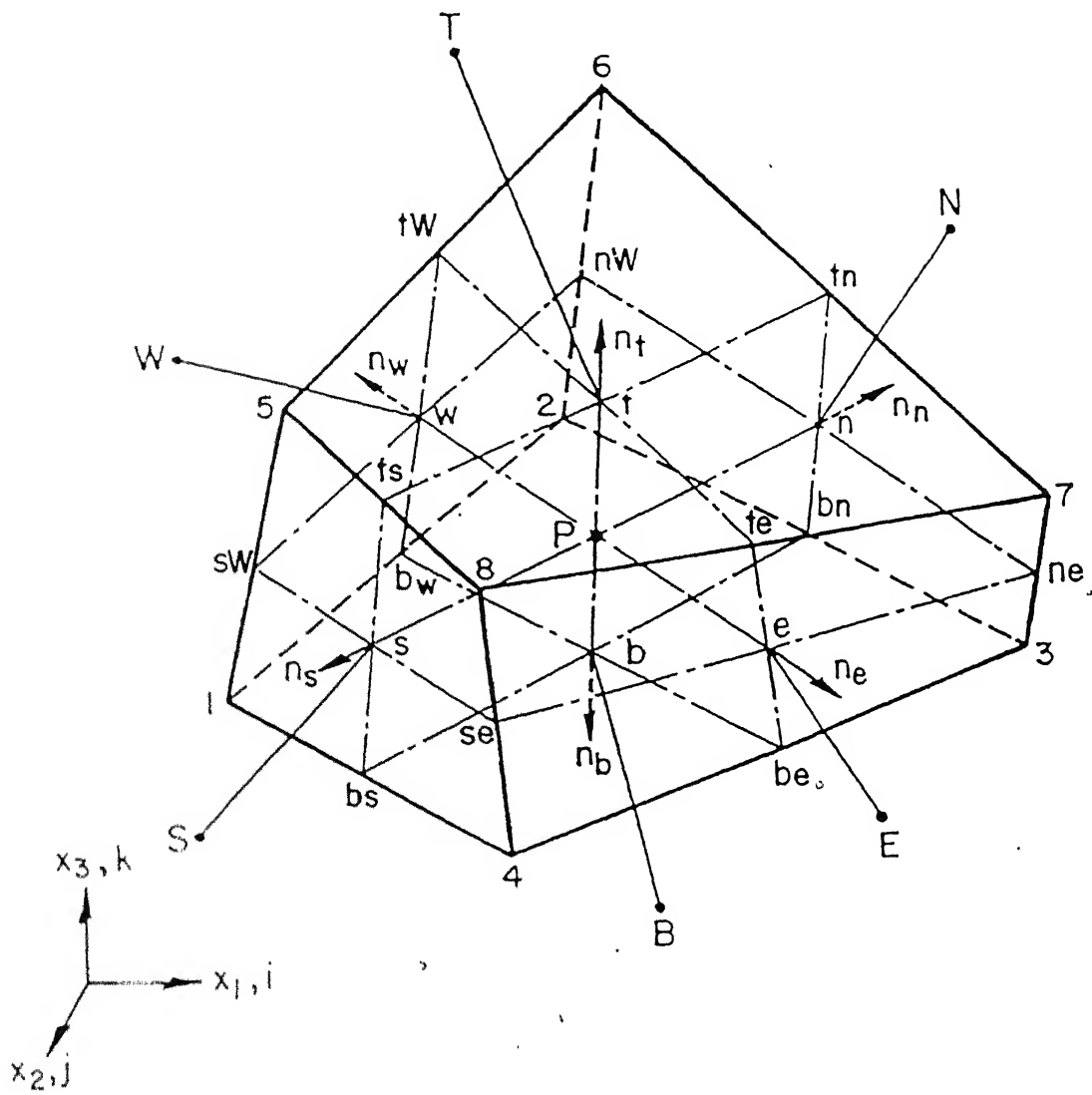
Figure 3.3   Three-Dimensional finite volume cells
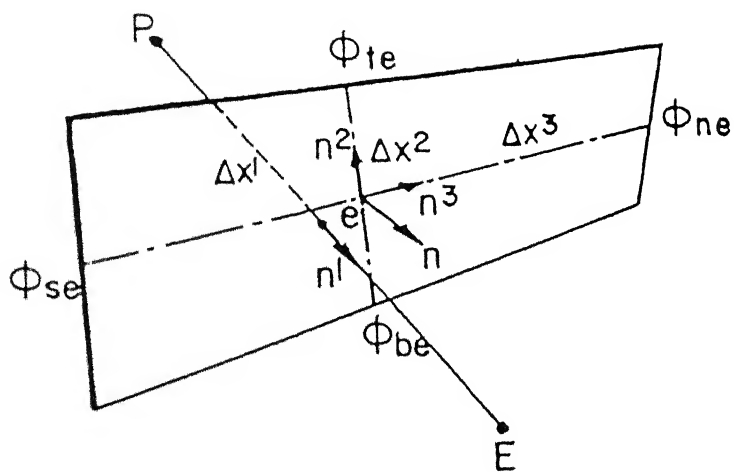
Figure 3.4   Face representation to illustrate diffusion model

```
                      ┌─────────────┐
                      │    START    │
                      └──────┬──────┘
                             │
                             ▼
              ┌──────────────────────────────┐
              │ Initialization:              │
              │   • Grid Data                │
              │   • Initial                  │
              │     Condition                │
              │   • Fluid Properties         │
              └──────────────┬───────────────┘
                             │
                             ▼
          ┌──────────────────────────────────────┐
          │   • Solve Momentum Equations         │
          │   • Obtain the Predictor Velocities  │
          └──────────────────┬───────────────────┘
                             │
                             ▼
      ┌──────────────────────────────────────────────────┐
      │  • Solve the Mass Balance (Pressure Correction    │
      │    Equation)                                      │
      └──────────────────┬───────────────────────────────┘
                             │
                             ▼
      ┌──────────────────────────────────────────────────┐
      │   • Correction of Velocity Components and Pressure│
      └──────────────────┬───────────────────────────────┘
                             │
                             ▼
          ┌──────────────────────────────────────┐
          │   • Solve the Temperature Equation   │
          │   • Update the Temperature Field     │
          └──────────────────┬───────────────────┘
                             │
                             ▼
                         ◇ Check
                No ◀───── Convergence
                         for Steady
                         State State ◇
                             │
                            Yes
                             │
                             ▼
                      ┌─────────────┐
                      │     END     │
                      └─────────────┘
```
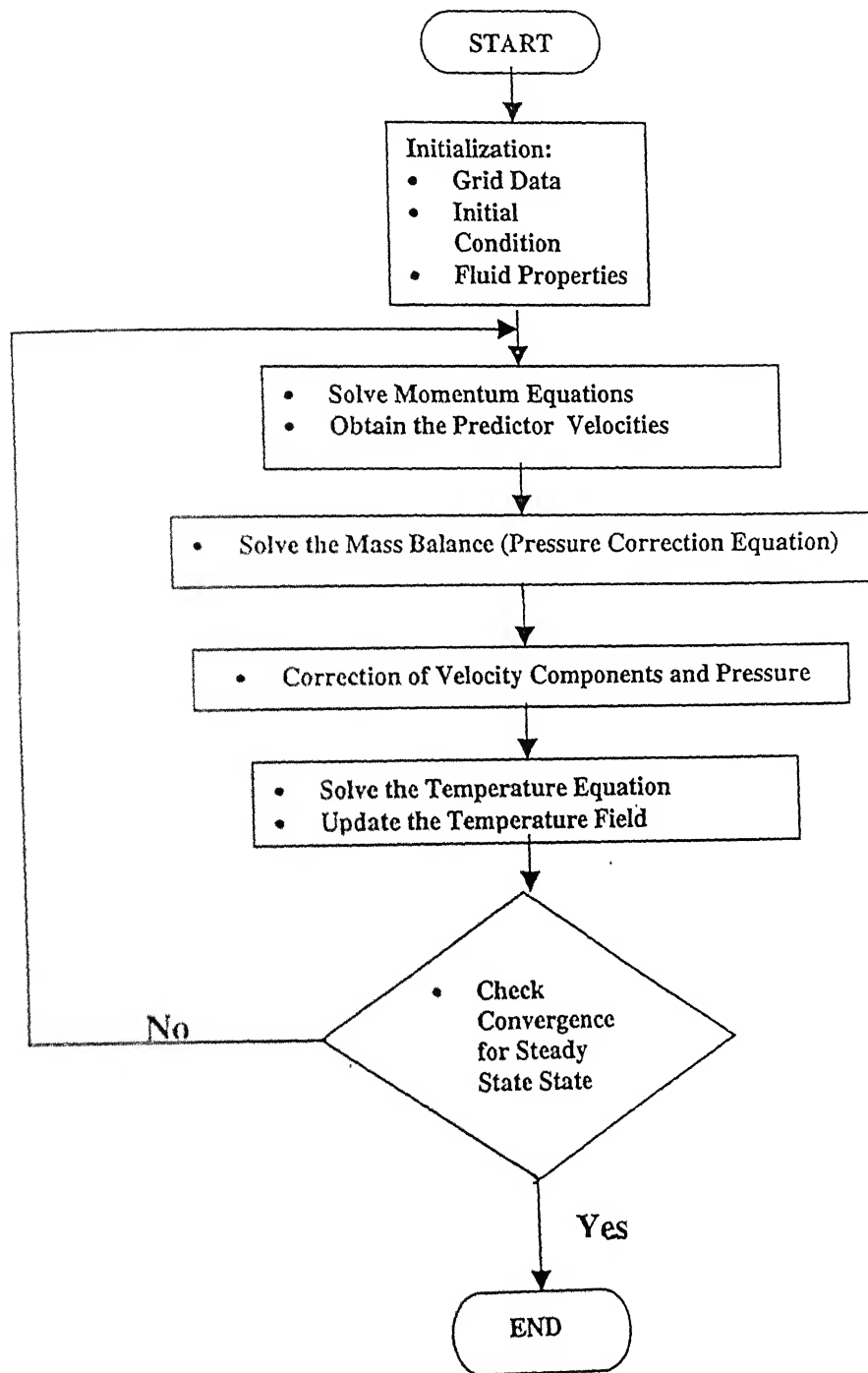
Figure 3.5   Flowchart of iterative solution scheme

Chapter 4
RESULT AND DISCUSSION

4.1   Introduction

A 62 × 61× 19 three-dimensional grid-mesh is used for the numerical study of flow and heat transfer in a channel with built-in oval-tube and delta winglet-type vortex generators in common-flow-down and common-flow-up configurations. The present computations are carried out for different angles of attack, various positions of the winglets and different Reynolds numbers. The divergence free criterion is satisfied with an upper bound of 10^{-4}. The blockage ratio (ratio of the minor diameter of oval tube to the width of channel) is 0.26. Air has been taken as the working fluid; hence the Prandtl number of the present study is 0.7. Span-averaged Nusselt number $(\overline{Nu_s})$, based on the bulk mean temperature, has been used for comparing the heat transfer performance.

4.2   Flow characteristics

This section deals with the flow characteristics for the flow in a rectangular channel with built-in oval tube and winglet pairs. The results presented here correspond to Re = 1000, Pr = 0.7 and $\beta = 40^0$.

4.2.1 Flow past an oval tube

Figure 4.1 shows the limiting streamlines for the time-averaged flow through a rectangular channel with built-in oval tube, in the region close to the bottom plate. Saddle point of separation and a horseshoe vortex system is observed in the figure. The incoming flow does not separate as in usual manner but reaches a stagnation or saddle point of separation (marked A) and goes around the tube. The nodal point of attachment is marked as B. The separation lines form elliptical arcs along the tubes. As the fluid approaches the stagnation line of the oval tube, its velocity head contributes to total pressure. The velocity in the boundary layer on

39

the channel walls increases in the vertical direction away from walls. This results in smaller total pressure on the stagnation line, close to the bottom wall. Thus a pressure gradient is set on the stagnation line that causes flow towards the channel walls. The fluid rolls up forming vortices, which are swept around the oval tube base and are carried downstream. This results in formation of horseshoe vortices on the sides of the oval tube. The symbol C marks the traces of the horseshoe vortices in the figure. An arch vortex (marked as D) is observed behind the tube.

Figure 4.2 shows the streamlines for the time-averaged velocity field on the horizontal mid-plane for the flow through a rectangular channel with built-in oval tube. The two symmetrical standing vortices, known as von Karman vortices, are observed from the figure. The recirculation in the wake region of the tube is clearly established. As compared to a circular tube, oval tube is a more streamlined body, so there is considerable delay in separation and wake zone is quite narrow.

4.2.2 Effect of winglets on flow structure

Figure 4.3 shows how the longitudinal vortices are generated by the winglet. It generates two types of vortices, such as, main vortices and the horseshoe vortices. Horseshoe vortices are induced due to velocity variation in boundary layer over the base plate. The mechanism is similar to the formation of horseshoe vortex system for the case of flow past an oval tube as explained earlier. The main vortices are created due to the pressure difference between the front surface facing the flow and the suction surface of the winglets.

Figure 4.4 shows limiting streamlines for the flow through rectangular channel with built-in oval tube and one winglet pair in common-flow-down configuration, on a plane close to the bottom plate. The winglets generate longitudinal vortices in the downstream. The saddle point of separation and the nodal point of attachment are visible in the figure. The wake is symmetric at this stage. The

twisted streamlines, near the winglets are the footprints of the swirling motion, which has a dominant component in the transverse direction. The transverse momentum transfer to the near field boundary layer of the aft region of the oval tube delays the separation.

Figure 4.5 show the limiting streamlines for the flow through a rectangular channel with built in oval tube and two winglet pairs. Both winglets have identical geometrical parameters but are placed simultaneously in two different orientations (common-flow-down and common-flow-up). The saddle point of separation is observed before the tube. The nodal points of attachment and separation lines are clearly visible. In further downstream, wake stagnation point is located. The wake is symmetric at this stage. The twisted streamlines near the winglets show the existence of strong swirling motion, which helps in delaying separation.

Figure 4.6 and Figure 4.7 show the velocity vectors and the streamlines on the various cross-stream planes for the flow through a rectangular channel with a built-in oval tube and one delta winglet pair in common-flow-down configuration. Figures 4.6(a) and 4.7(a) are at the location X = 1.75 which is on the winglet. Figures 4.6(b) and 4.7(b) are at the location X = 3.61, just after the winglet. Figures 4.6(c) and 4.7(c) are at the location X = 5.48, downstream of the winglet. All these axial locations are measured from the channel inlet. Each winglet pair produces two vortices: a main vortex and a corner (horseshoe) vortex. Mendez et al. (1998) have explained the kinematics of flow and mechanism of transport enhancement due to interaction of the vortices. The main (primary) vortices and horseshoe vortices constitute longitudinal vortices, since the axes of the vortices are parallel to the main flow direction. Vortex interaction with common flow between the vortices directed towards the wall has been extensively studied by Pauley and Eaton (1998). The downwash causes strongest distortion of the boundary layer over the streamwise distance. Outward in the span wise direction from the side of the tube, one encounters the horseshoe vortex due to the tube, the

primary vortex due to the winglet and the corner (horseshoe) vortex in the figure 4.7(c). The numerical flow visualization is well supported by the experiments of O'Brien et al. (2000).

Figure 4.8 and Figure 4.9 shows the velocity vectors and streamlines respectively for the flow through a rectangular channel with built-in oval tube and two winglet pairs, in common-flow-down and common-flow-up configurations. Velocity vectors and streamlines are drawn at four different axial locations, such as, at X = 2.68, 4.55, 6.41 and 9.21 respectively. In Figures 4.8(a) and 4.9(a), the main (primary) vortices due to the first winglet pair are clearly visible. Its strength increases as we move toward the trailing edge of the first pair of winglet. The formation of primary vortices due to second pair of winglets is also seen in Figures 4.8 (b) and 4.9(b). Figures 4.8(c) and 4.9(c) show the formation of horseshoe vortex system around the tube, and the main vortices due to first and second winglet pair. Here the strength of vortices due to second pair of winglet is more as compared to figures 4.8(b) and 4.9(b). The corner (horseshoe) vortices due to the second winglet pair become visible in Figures 4.8 (d) and 4.9(d). The streamlines confirm the existence of a strong swirl.

4.3   Heat transfer characteristics

This section deals with the heat transfer characteristics for the flow through a rectangular channel with built-in oval tube. Subsequently the conclusions are drawn about the effect of winglet pairs on heat transfer. The results are computed at Re = 1000, Pr = 0.7. The Nusselt number is calculated based on the bulk mean temperature. The oval tube and winglet pairs are assumed to be at the wall temperature.

4.3.1 Heat transfer in a channel with a built-in oval tube

Figure 4.10 represents local Nusselt number distribution on the bottom plate of the channel. At the leading edge of the channel, cooler fluid comes in contact with

the fin surface first time, so the local Nusselt number is high everywhere in the span wise direction. The gradual decrease in Nusselt number is attributed to the growth of boundary layer on the channel wall. An abrupt change in Nusselt number in the front the oval tube is observed. As the fluid approaches the stagnation line of the oval tube, it slows down and the pressure on the stagnation line increases. The smaller velocity in the boundary layer in the vicinity of the bottom plate, which supports the oval tube, leads a small pressure increase on the stagnation line. Thus, the induced pressure gradient on the stagnation line causes the flow towards the bottom wall and virtually impinges on the wall. The fluid rolls up forming vortices, which interacts with the main stream and finally wraps around the front half of the tube and extends to the rear of the tube. The fluid motion thus entails a horseshoe vortex system. The swirling action of the horseshoe vortices brings about a better mixing and the heat transfer in the neighborhood is enhanced significantly. The Nusselt number is again low in the wake region as shown in the figure. This is due to separated dead water zone with recirculating fluid at a low velocity.

4.3.2 Effect of winglet pair on heat transfer

Figure 4.11 shows the distribution of local Nusselt number on the bottom plate of the channel with a built-in oval tube and a winglet pair in front of the tube with common-flow-down configuration. At the leading edge of the channel and near the oval tube, the local Nusselt number distribution depicts the same trend as the earlier case for the reasons explained therein. The heat transfer enhancement associated due to the winglet pair is evident in the figure. Downstream of each winglet is strongly influenced by the swirling motion and the effect persists over a non-dimensional distance of 8 (eight). The heat transfer enhancement associated with the corner (horseshoe) vortex of each winglet is visible in the figure as a streak that begins on the upstream side of the winglet and is swept downstream wrapping the winglet.

Figure 4.12 shows the iso-Nusselt number distribution on the bottom plate of the channel for two winglet pairs deployed in the leading-edge region of the oval tube in a staggered configuration. The inner pair is in common-flow-down orientation and the outer pair is in common-flow-up orientation. Local regions of high heat transfer associated with the tube stagnation region, the tube horseshoe vortex, and the main (primary) and corner (horseshoe) vortices produced by each winglet are visible in the figure.

Figure 4.13 compares span-averaged Nusselt number distribution at the bottom plate of the channel for the cases of (a) rectangular channel, (b) channel with built in oval tube, (c) channel with built in oval tube and winglet pair with common-flow-down configuration and (d) channel with built in oval tube and winglet pairs with common-flow-down and common-flow-up configurations. For the case of a plane channel, the span-averaged Nusselt number starts with a very high value of 29.63 at the leading edge of the channel. Then the span-averaged Nusselt number decreases due to the growth of boundary layer, and finally it becomes almost constant (4.17) at the exit of the channel (curve a). In the case of built-in oval tube, there is an increase in the span-averaged Nusselt number at the axial location that corresponds to the leading edge of the oval tube. This is attributed to the formation of horseshoe vortices in front of the tube (curve b). The value of span-averaged Nusselt number at this location is 10.58. Curve c demonstrates the effect of winglet pair with common-flow-down configuration on the distribution of span-averaged Nusselt number. At the axial location corresponding to the location of trailing edge of the winglet ($X = 3.61$), the span-averaged Nusselt number reaches a very high value (11.18). This enhancement is about 81 percent higher as compared to the span-averaged Nusselt number for the plane channel at the same axial location. The span-averaged Nusselt number distribution shows remarkable improvement in the case of two winglet pairs (curve d). Maximum value of span-averaged Nusselt number (12.22) occurs at the axial location corresponding to the location of the trailing edge of the second winglet pair (with common-flow-up configuration). The location is at $X = 5.84$ and enhancement is

about 147 percent as compared to the span-averaged Nusselt number value for the plane channel at the same location. Table 4.1 compares the mean Nusselt number (global mean) for different obstacles used in this study.

Table 4.1

Configuration	Mean Nusselt number (global mean), Nu_m	% Nu_m enhancement
Plane Channel	6.67	----
Channel with built-in oval tube	7.82	17.24
Channel with built-in oval tube and one winglet pair	9.71	45.58
Channel with built-in oval tube and two winglet pairs	11.25	68.66

Figures 4.14 (a) and (b) show the variation of local Nusselt number along the span wise direction at the locations $X = 2.7$ and 4.26 respectively. Figure 4.14(a) shows two peaks on the either side of the oval tube. The peaks reveal the effect of the oval tube and the inner winglet pair with common-flow-down configuration. The first peak is the effect of formation of the complex longitudinal vortex system due to the winglet pair and the second peak is due to the horseshoe vortex system generated by the oval tube. Figure 4.14(b) shows the effect of two pairs of winglets, through the formation three peaks. The first peak is the effect of formation of the longitudinal vortex system due to the outer winglet pair with common-flow-up configuration while higher peak (second) is brought about by the longitudinal vortex system due to the inner winglets with common-flow-down configuration. The third peak near the oval tube is due to the horseshoe vortex system generated by the oval tube.

4.4 Comparison of Span-averaged Nusselt number for different Reynolds Number

Figure 4.15 shows the variation of span-averaged Nusselt number distribution in the flow direction at three different Reynolds numbers, such as, Re = 500, 1000, and 1500 for the one pair of winglet in common-flow-down configuration. The curves show the similar qualitative trend of variation. The span-averaged Nusselt number is high for the higher value of Reynolds number. Table 4.2 shows the value of span-averaged Nusselt numbers at the exit of the channel for different Reynolds numbers.

Table 4.2

Reynolds Number	Span-averaged Nu at the exit of the channel	Mean Nusselt Number, (global mean) Nu_m
500	4.54	6.71
1000	6.19	9.71
1500	6.97	11.42

4.5 Comparison of Span-averaged Nusselt Number for different angles of attack (β)

Figure 4.16 compares the span-averaged Nusselt number distribution in the channel with built-in oval tube and two winglet pairs. The Reynolds number of interest is 1000. These curves show similar qualitative trend. Winglets with higher angle of attack produce vortices with higher strength, which result in better heat transfer. Table 4.3 summarizes the effect of angle of attack on mean Nusselt Number (global mean), Nu_m on the bottom pate of the channel.

46

Table 4.3

Configuration	Mean Nusselt number (global mean), Nu_m	% Nu_m Enhancement
Without winglet pairs	7.82	----
$\beta = 30$	9.37	19.82
$\beta = 35$	10.00	27.88
$\beta = 40$	11.25	43.86

4.6 Comparison of Span-averaged Nusselt Number for Different Axial Locations of the Winglet pair

Figure 4.17 compares the span-averaged Nusselt number distribution on the bottom wall of the channel for different axial positions of the winglet pair. The results are for the winglets with common-flow-down configuration. The mean Nusselt number (global mean), Nu_m is 9.71 for the location of the leading edge of the winglet pair at $X / L = 0.119$. Likewise, Nu_m is 9.22 for the location of the leading edge of the winglet pair at $X/ L = 0.186$ and Nu_m is 9.23 for the location of the leading edge of the winglet pair at $X / L = 0.254$. This trend shows that for better heat transfer, winglets must be mounted on the fin surface near the leading edge of the oval tube.

4.7 Grid Independence Test

Figure 4.18 compares the span-averaged Nusselt number distribution on the bottom wall of the channel for three different grids for the flow through a channel with built in oval tube and winglet pairs with common-flow-down configuration. Three different grid-meshes, namely, $62 \times 61 \times 19$, $72 \times 71 \times 21$ and $82 \times 81 \times 25$ were utilized to test the grid sensitivity. The results reveal minor change (less than 4%) in span-averaged value of Nusselt number for different grids at any axial location in the channel.
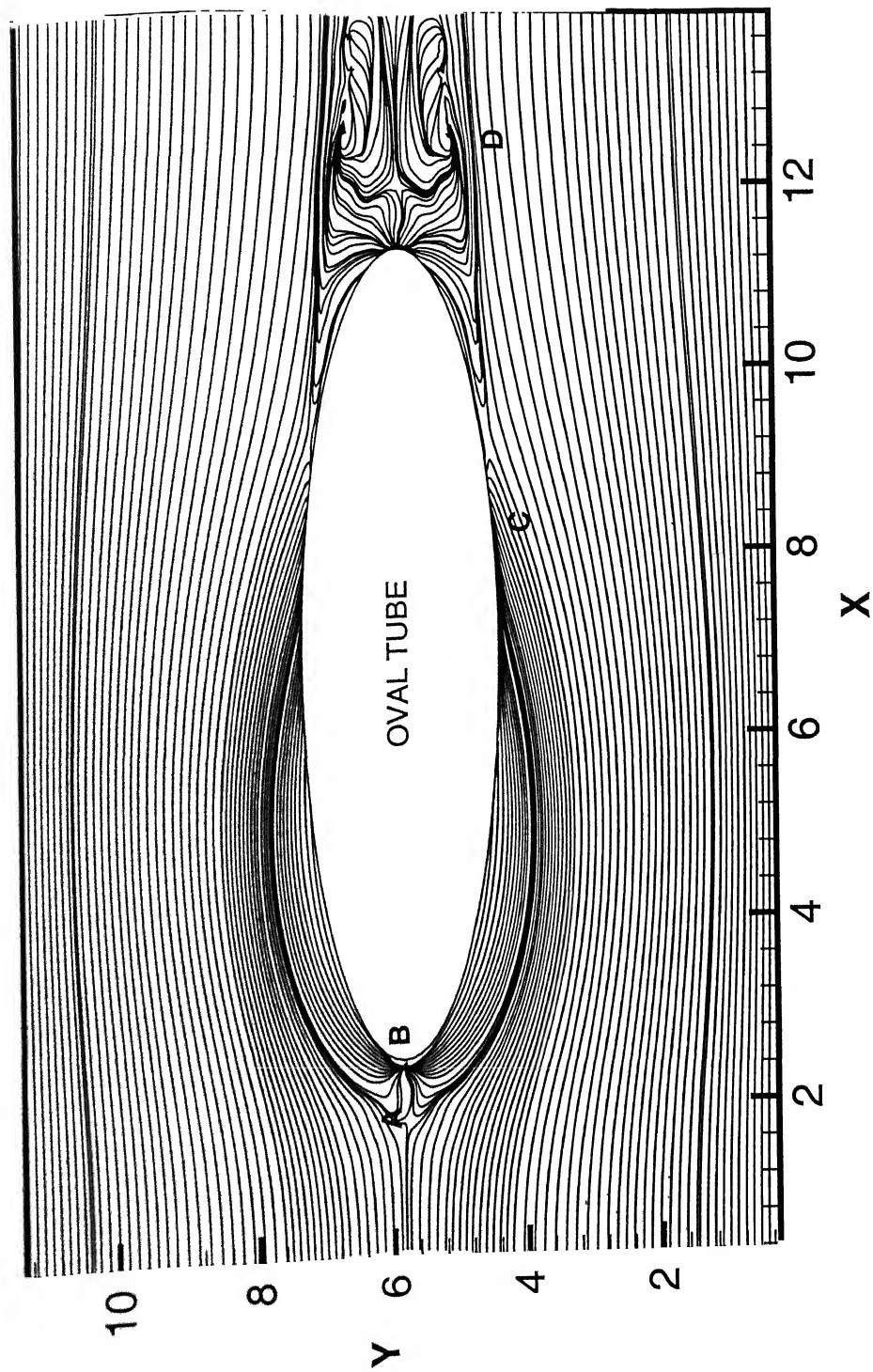
Re = 1000   Pr = 0.7

OVAL TUBE

Figure 4.1   Limiting streamlines at on a plane close to the bottom plate for the case of
flow through a channel with built-in oval tube

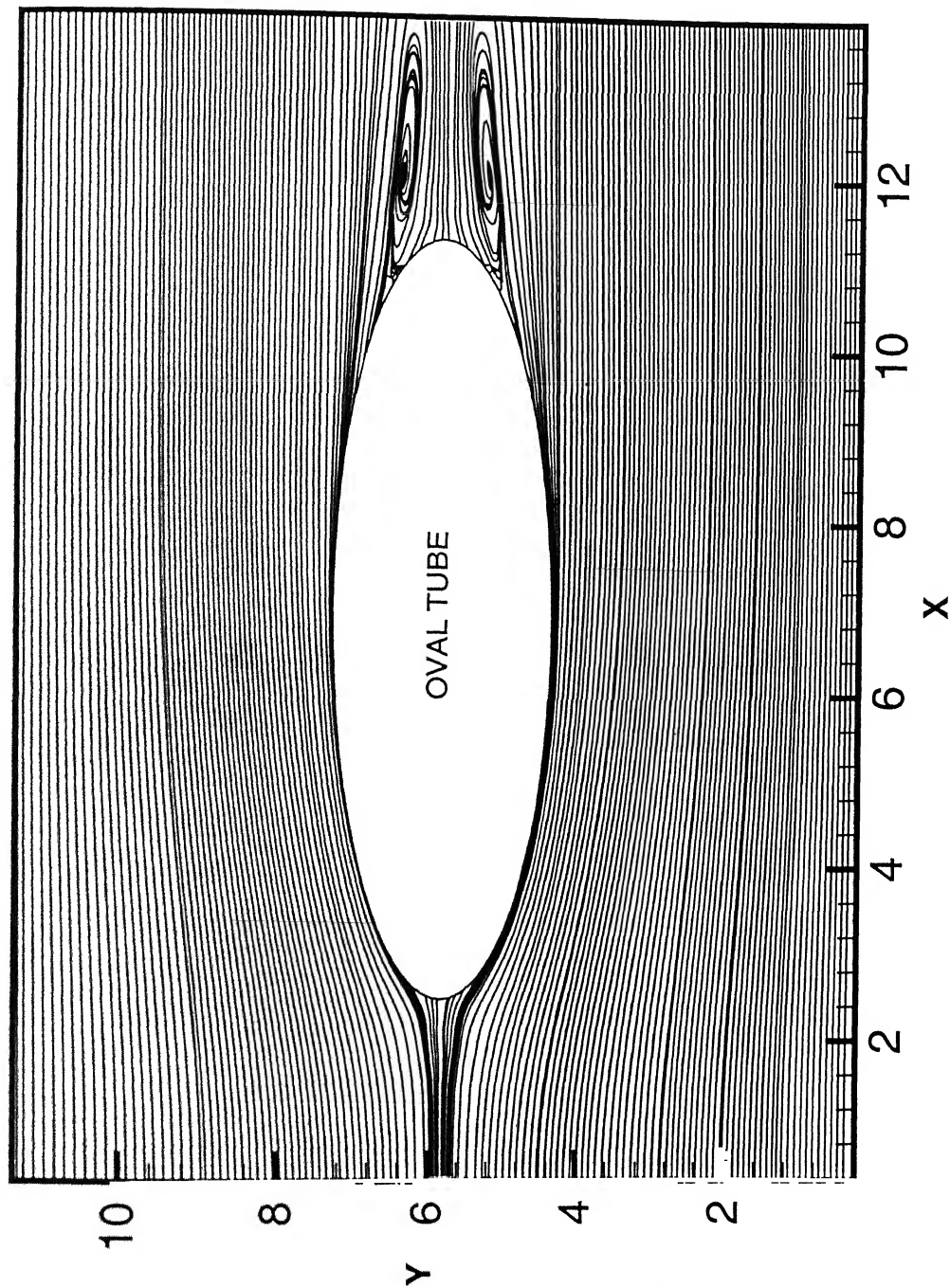Re = 1000   Pr = 0.7

OVAL TUBE

Y

X

Figure 4.2   Streamlines plot on a horizontal mid-plane for the case of flow through a channel with built-in oval tube
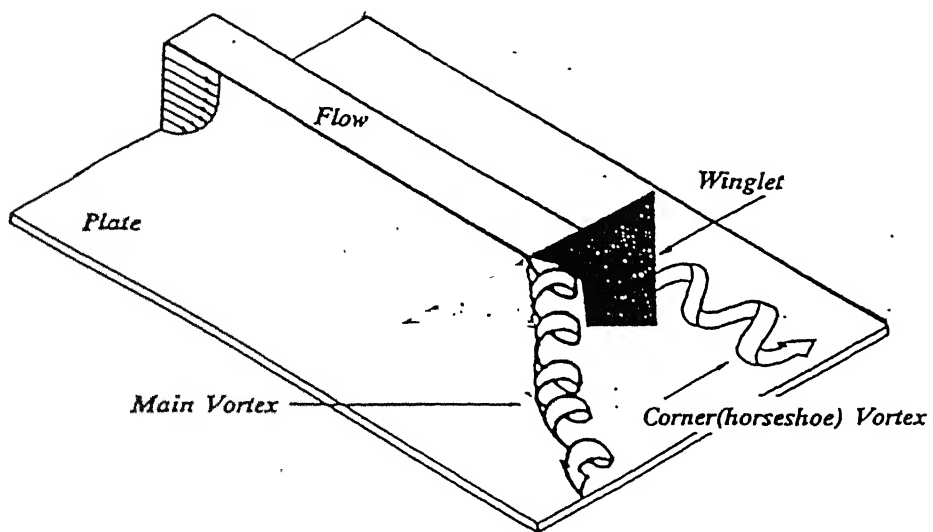
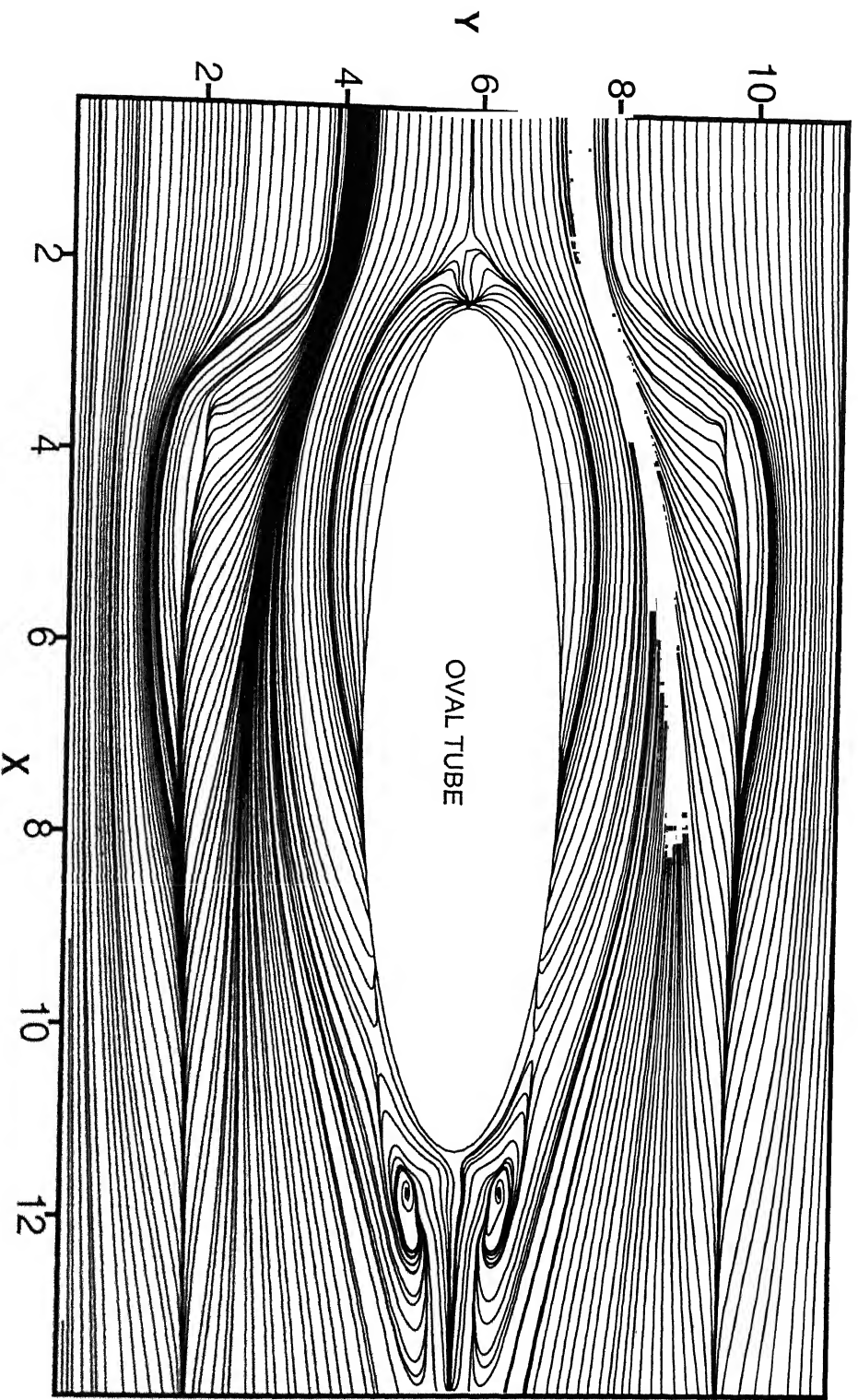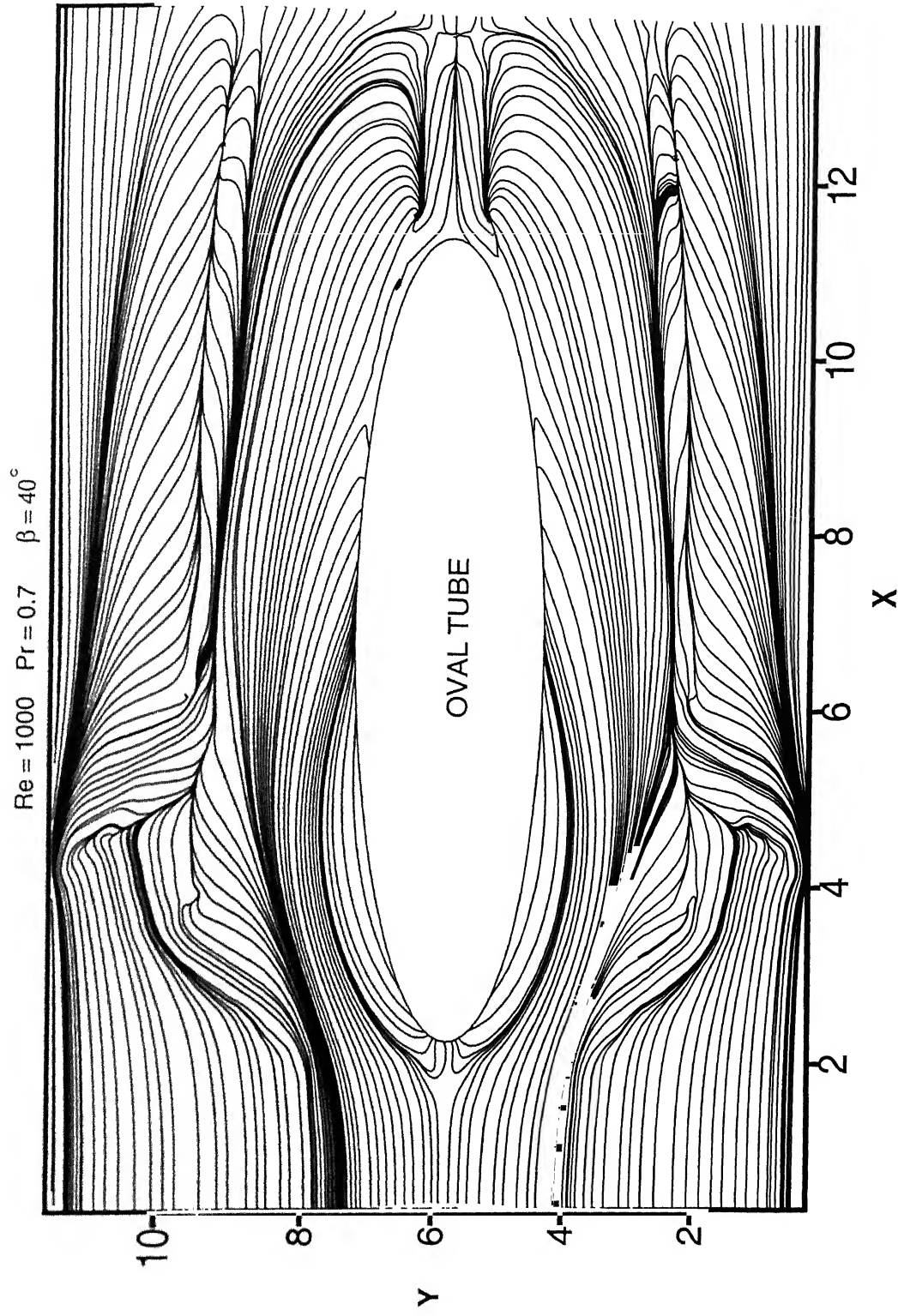Figure 4.3   Formation of Vortices due to Winglet

Re = 1000   Pr = 0.7   β = 40°

OVAL TUBE

Figure 4.4   Limiting streamlines on a plane close to the bottom plate for the case of
flow through a channel with built-in tube and one winglet pair

Re = 1000   Pr = 0.7 $\beta = 40°$

OVAL TUBE

X

Y

Figure 4.5   Streamlines on a plane close to the bottom plate for the case of flow
through a channel with built-in tube and two winglet pairs
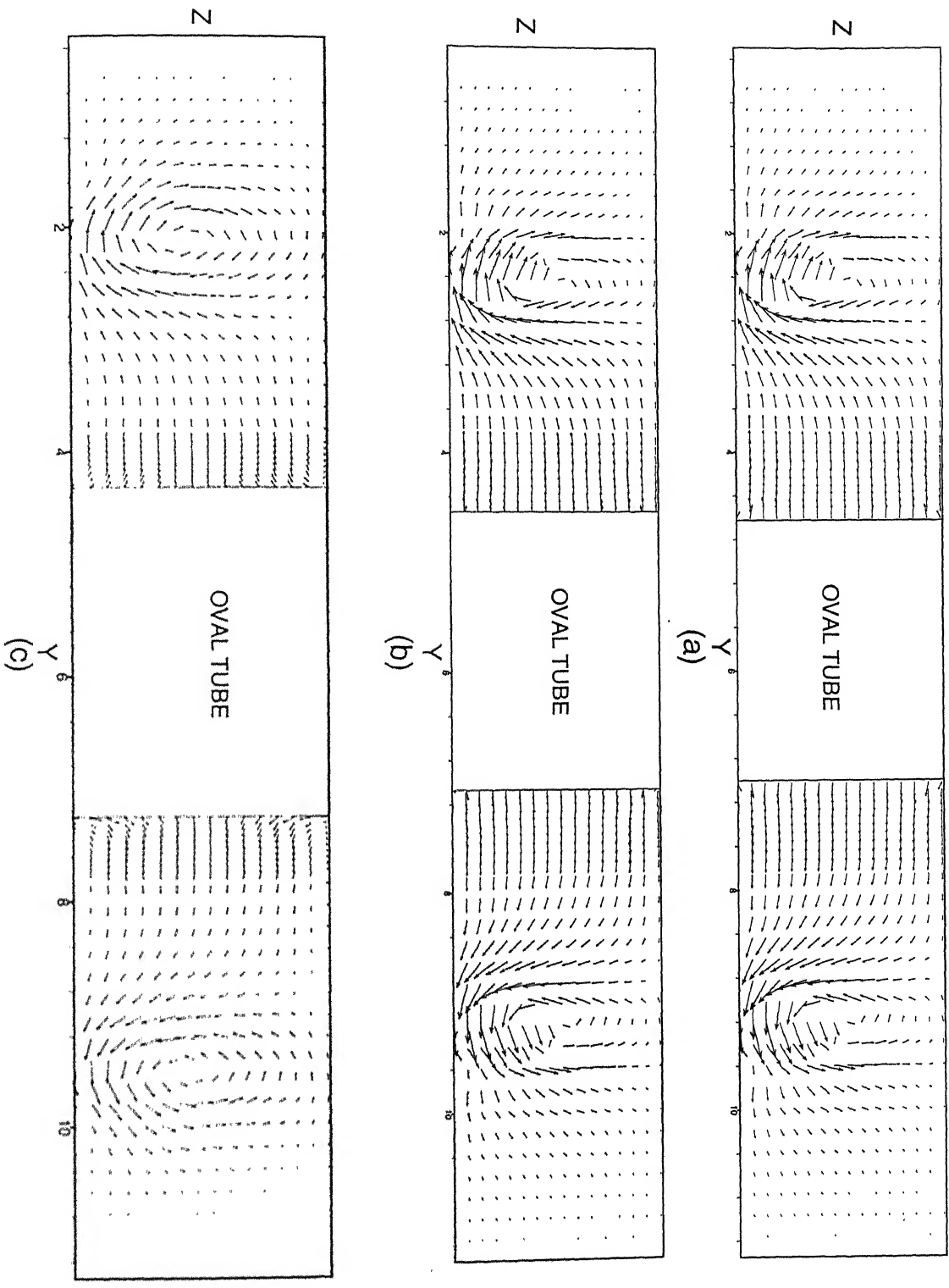
Figure 4.6   Velocity vectors in cross plane at various x-locations for one winglet pair

(a) X = 1.75, (b) X = 3.61 and (c) X = 5.48
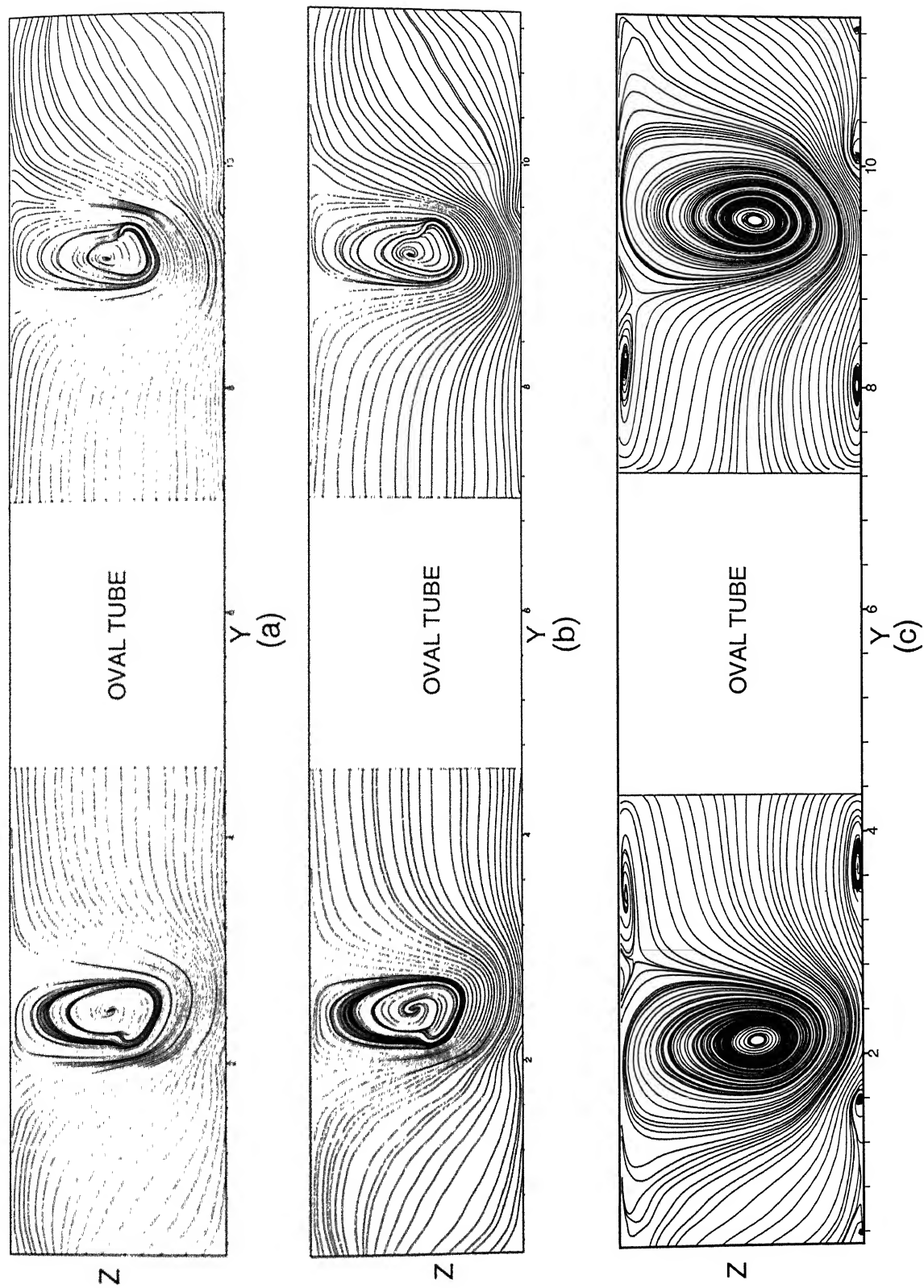
Figure 4.7   Streamlines in cross plane at various x-locations for one winglet pair
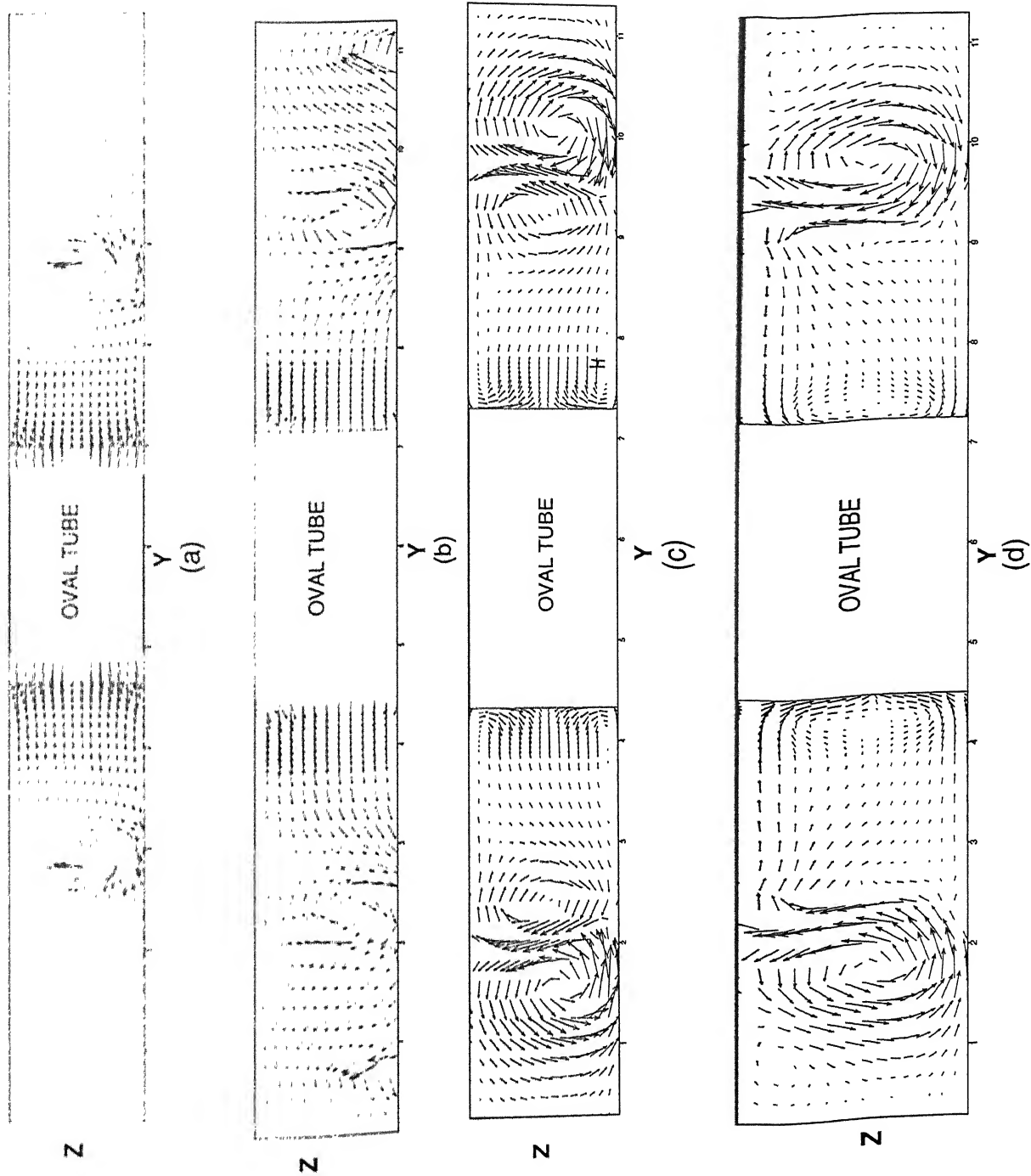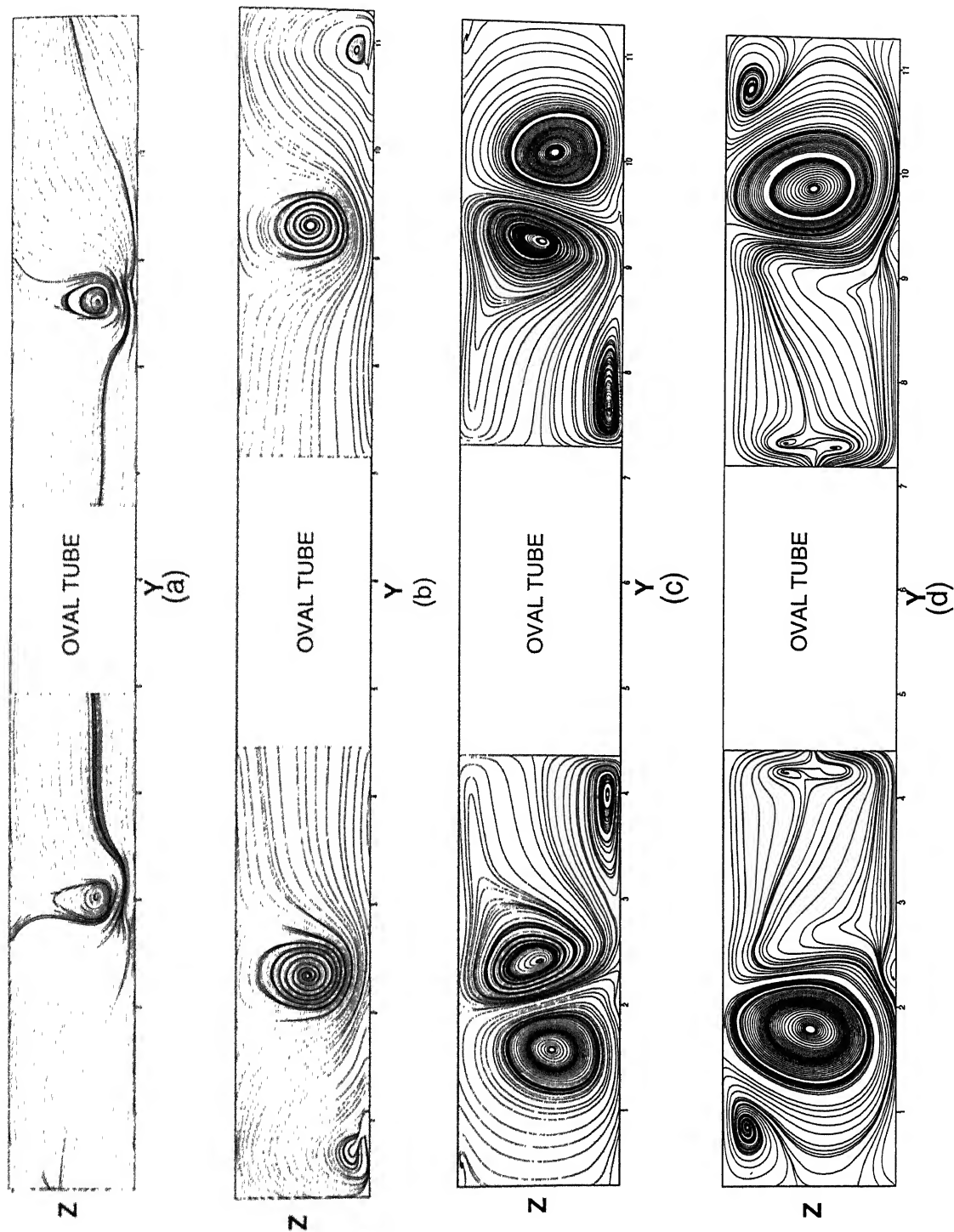
(a) X = 1.75, (b) X = 3.61 and (c) X = 5.48

OVAL TUBE

Z

Y
(a)

OVAL TUBE

Z

Y
(b)

OVAL TUBE

Z

Y
(c)

OVAL TUBE

Z

Y
(d)

Figure 4.8   Velocity vectors in cross plane at various x-locations for two winglet pairs

Figure 4.9   Streamlines in cross plane at various x-locations for two winglet pairs

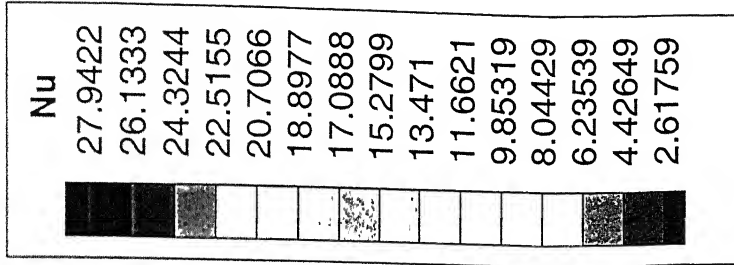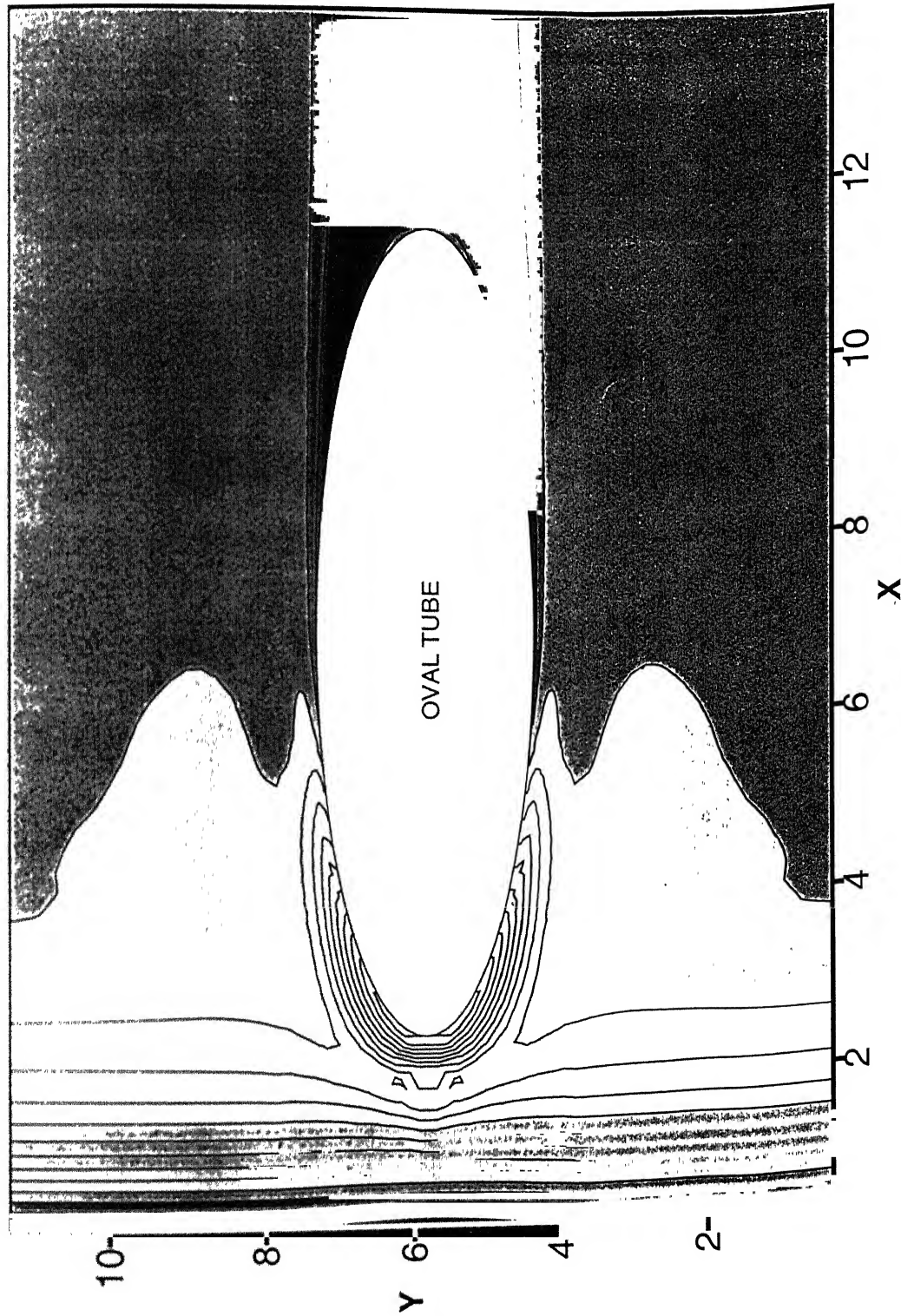(a) X = 2.68, (b) X = 4.55, (c) X = 6.41 and (d) X = 9.21

Re = 1000   Pr = 0.7

Nu
27.9422
26.1333
24.3244
22.5155
20.7066
18.8977
17.0888
15.2799
13.471
11.6621
9.85319
8.04429
6.23539
4.42649
2.61759

OVAL TUBE

Figure 4.10   Iso-Nusselt number distribution on the bottom plate for the case of flow

through a channel with built-in oval tube

Nu

27.8569
25.9658
24.0747
22.1835
20.2924
18.4013
16.5101
14.619
12.7279
10.8367
8.94559
7.05445
5.16332
3.27218
1.38105

Re = 1000   Pr = 0.7   β = 40

OVAL TUBE

12   10   8   6   4   2

X

10   8   6   4   2

Y

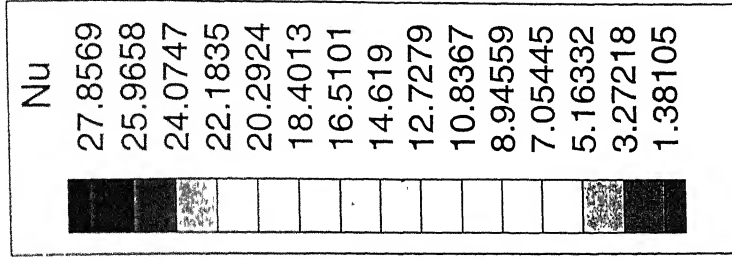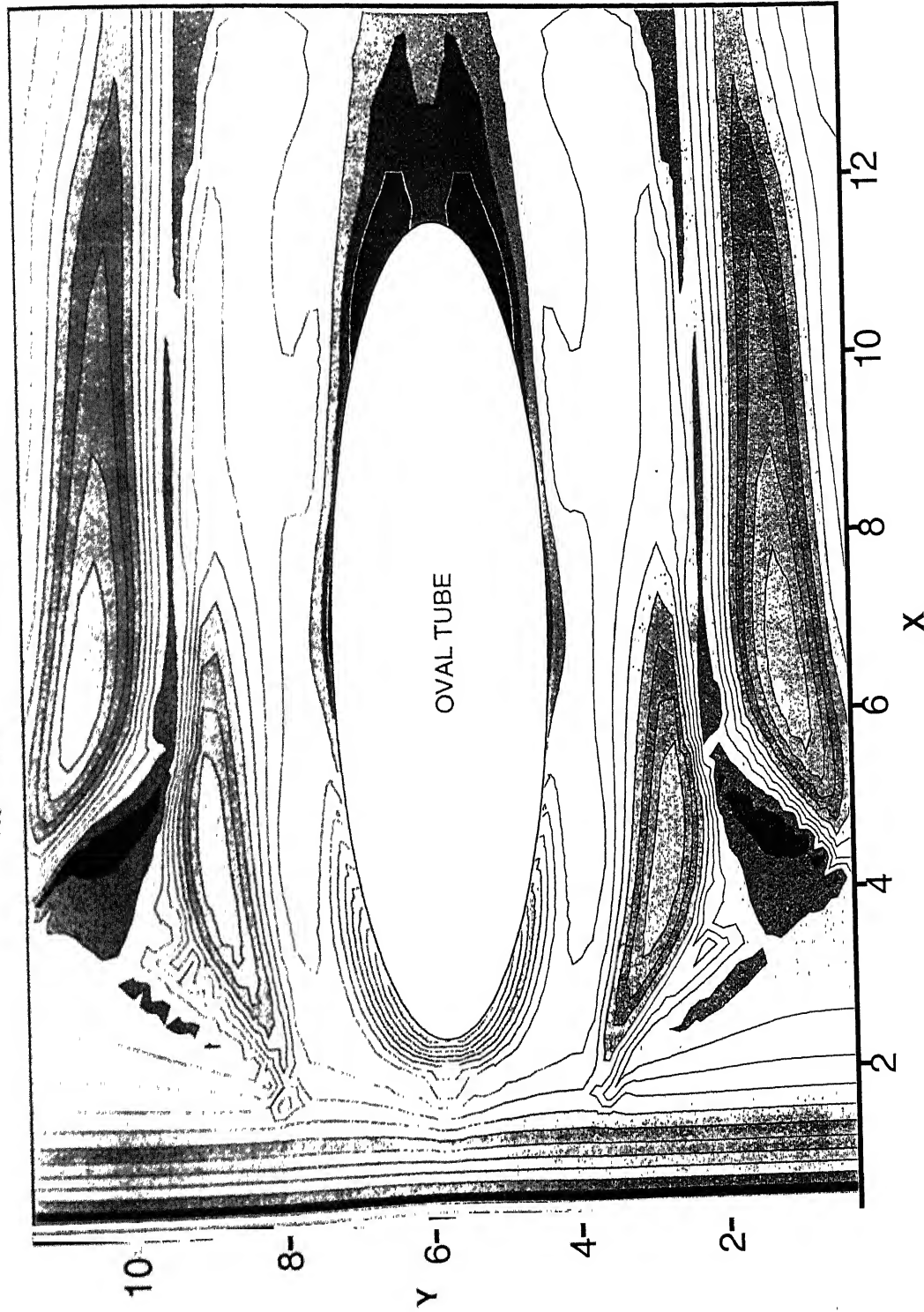Figure 4.12   Iso-Nusselt number distribution on the bottom plate for the case of flow
through a channel with built-in oval tube and two winglet pairs
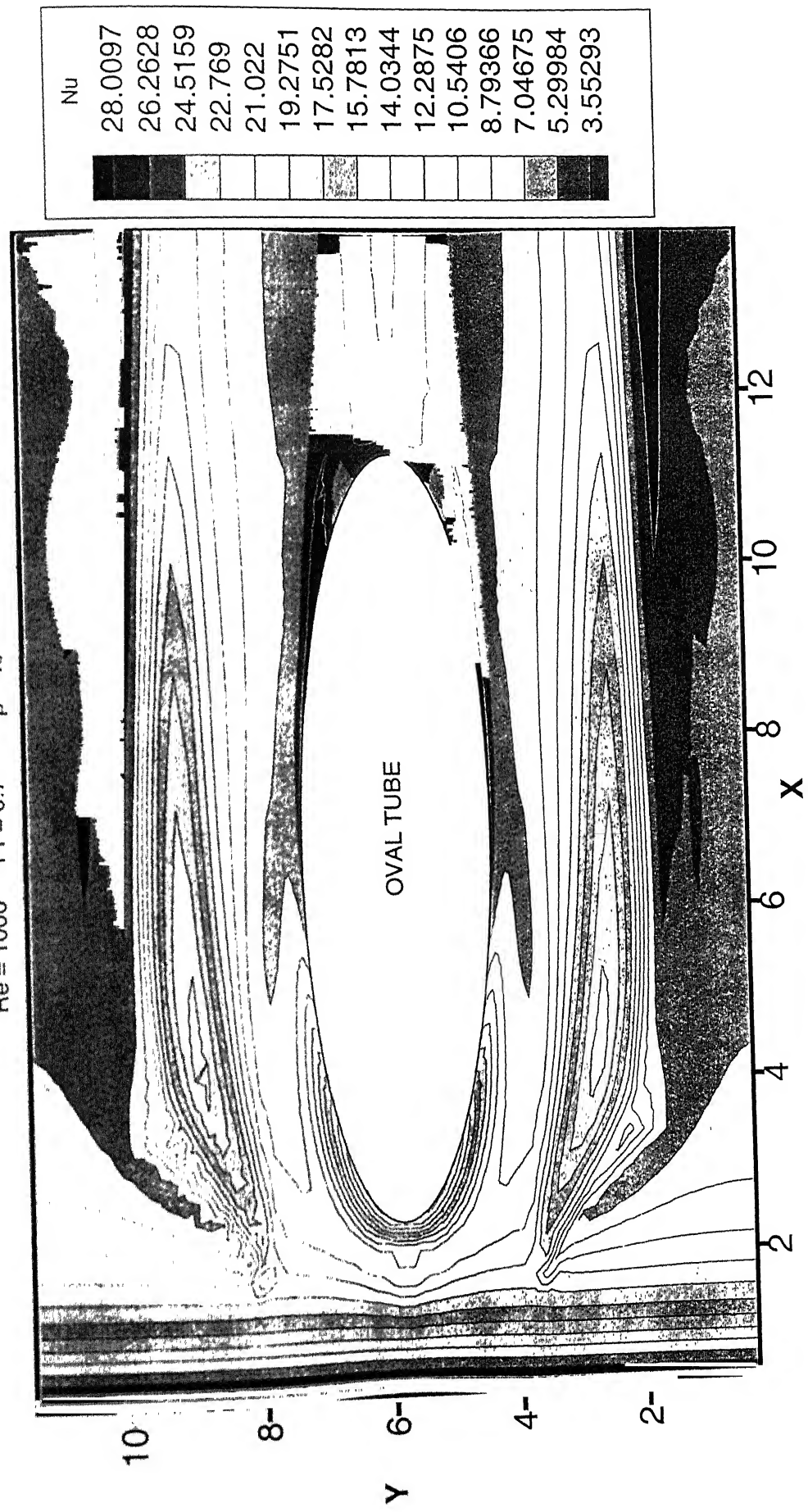
Figure 4.11   Iso-Nusselt number distribution on the bottom plate for the case of flow
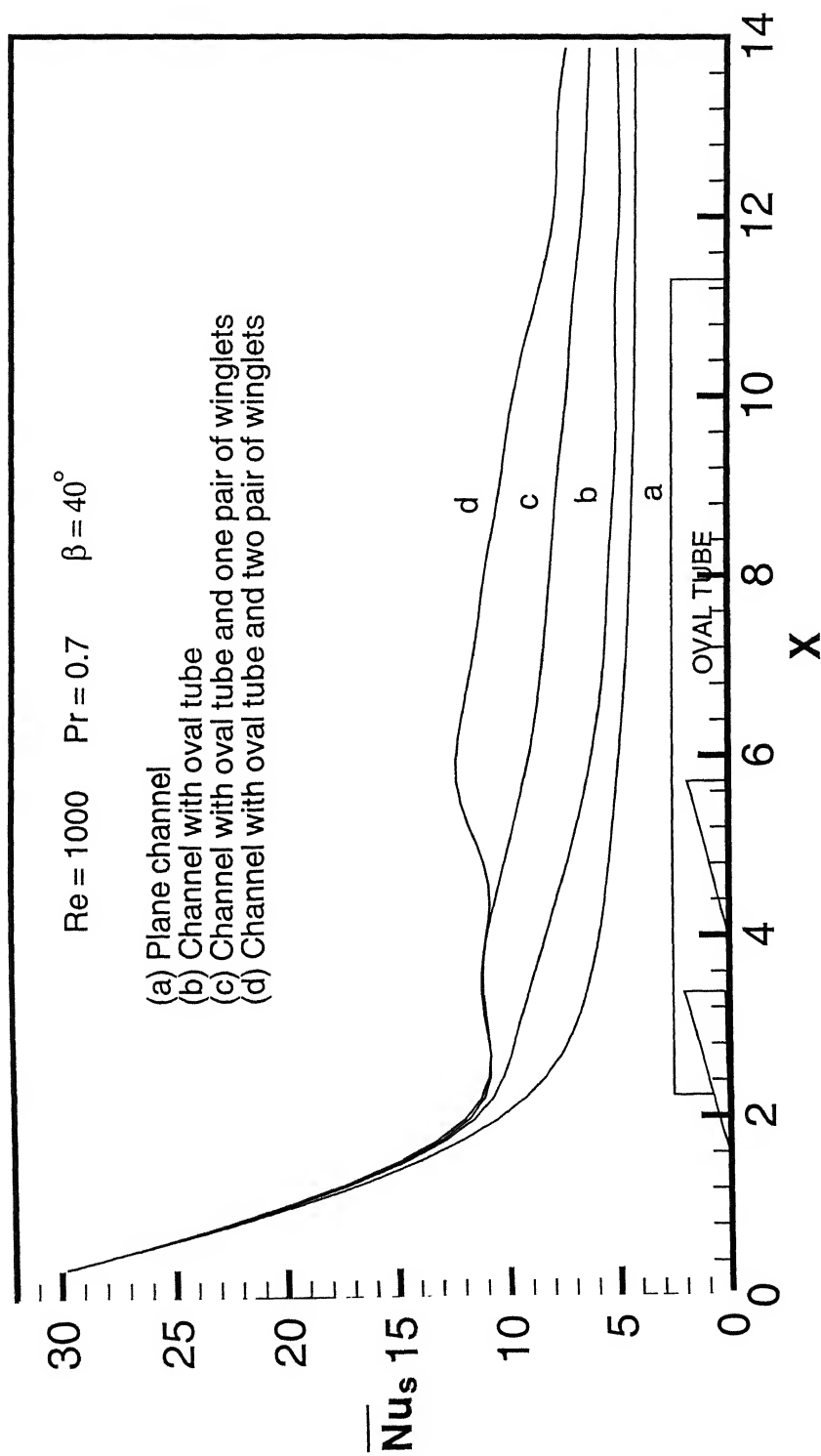through a channel with built-in oval tube and one winglet pair

Figure 4.13   Comparison of span averaged Nusselt number for channel, channel with
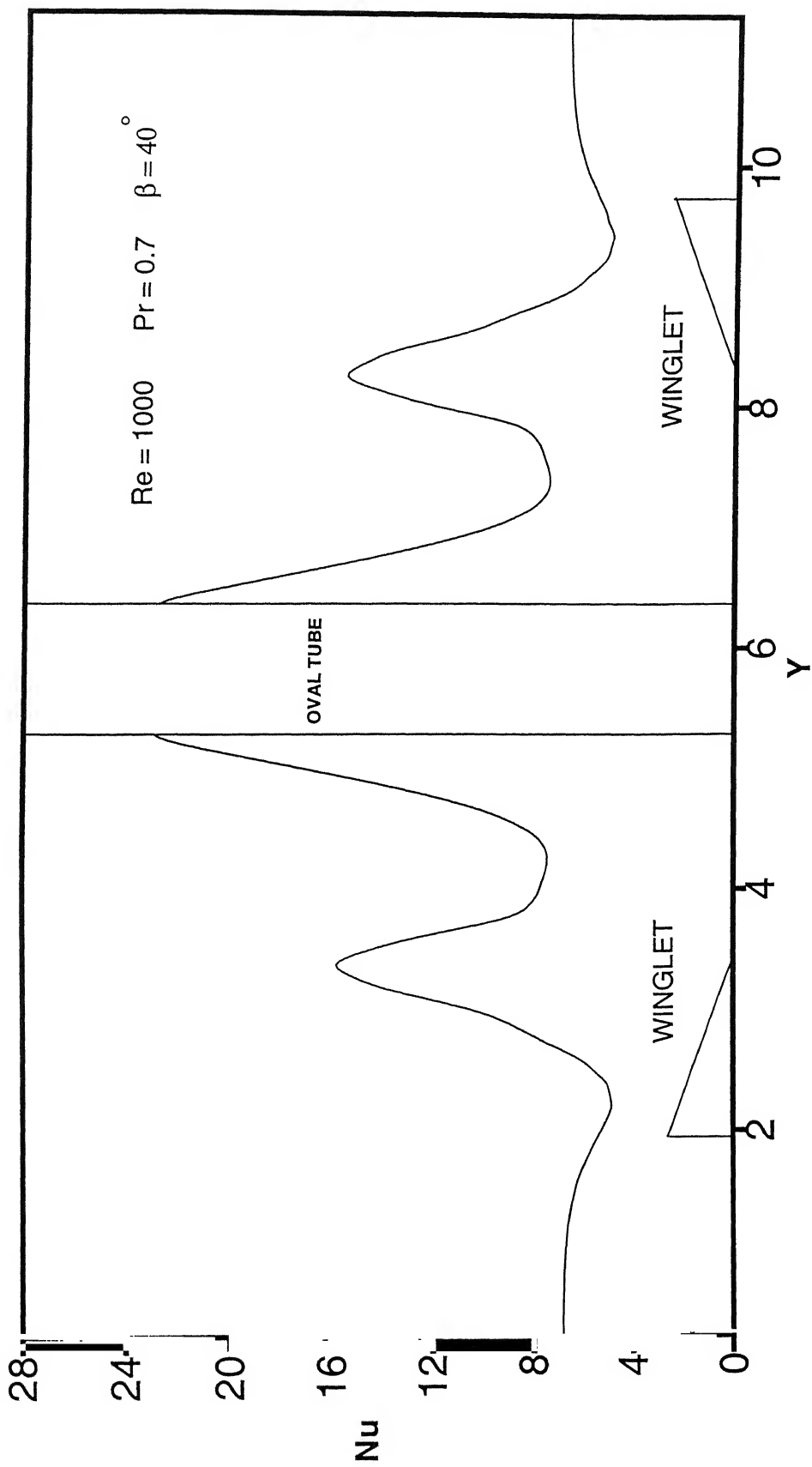oval tube, channel with oval tube and winglet pairs

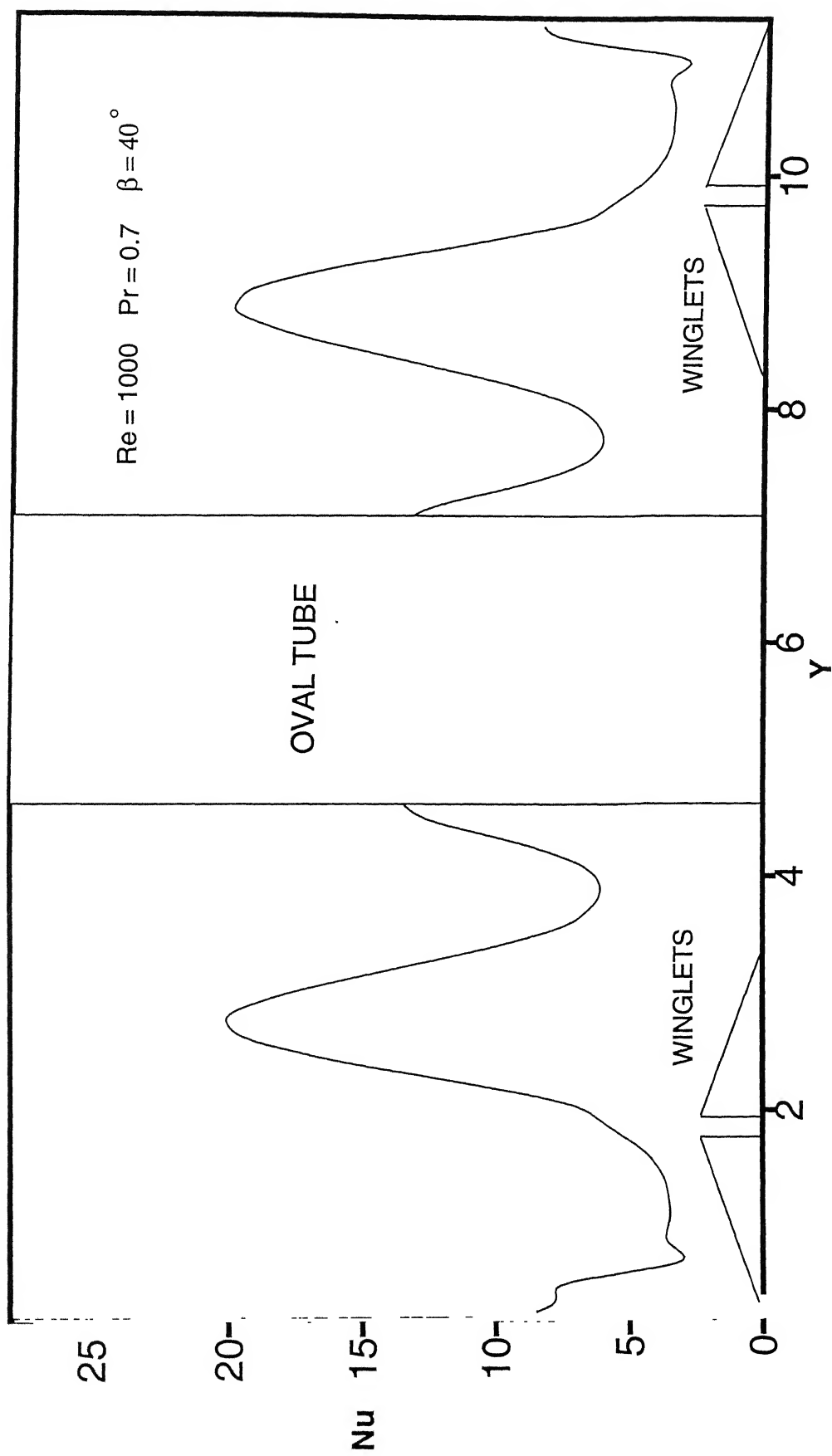Figure 4.14   (a)   Spanwise variation of Nusselt number at location x = 2.7

Figure 4.14 (b) Spanwise variation of Nusselt number at location x = 4.26

For channel with oval tube and one pair of winglets
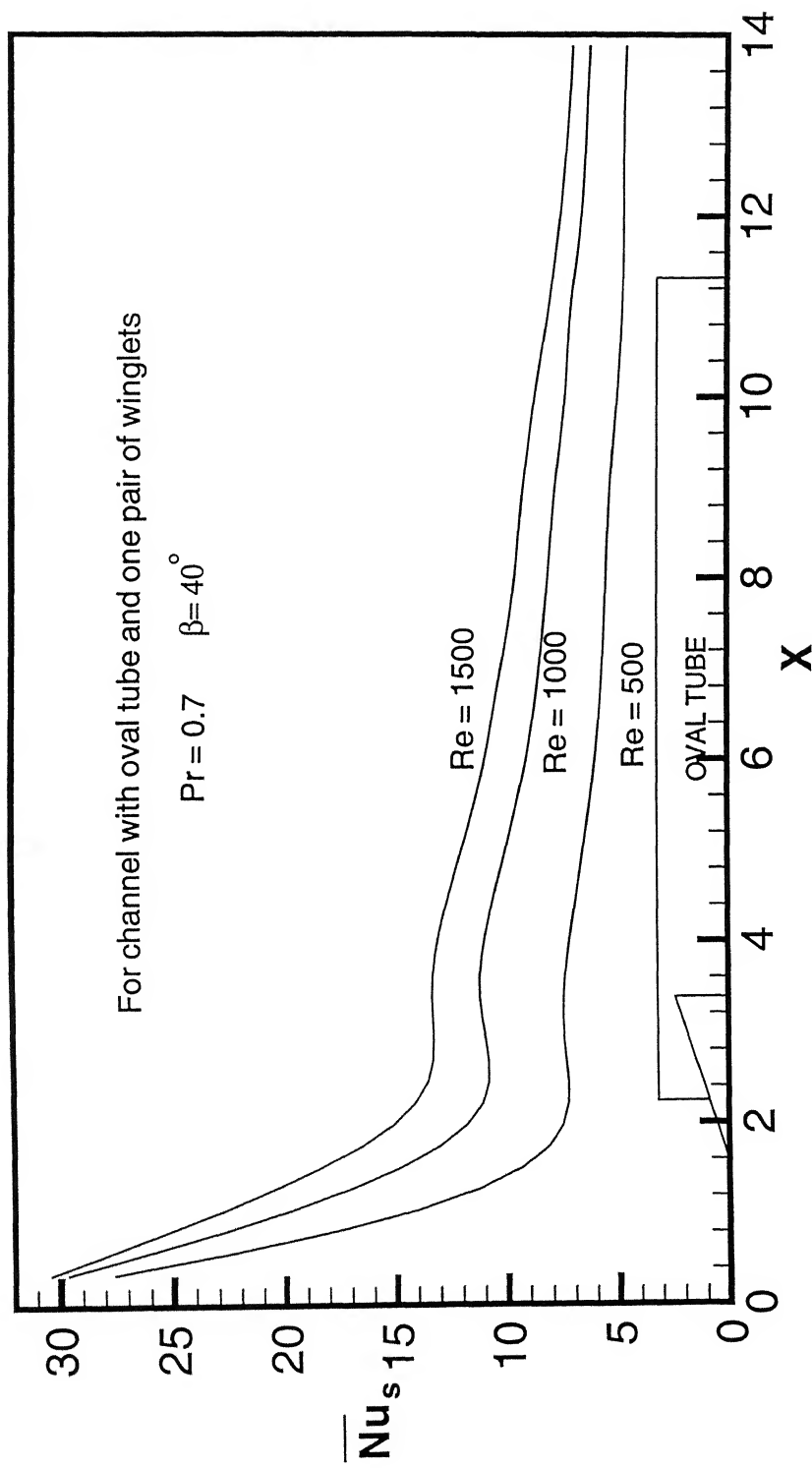
$Pr = 0.7$ $\quad \beta = 40°$

Figure 4.15 Comparison of span averaged Nusselt number for different Reynolds number for the case of flow through channel with oval tube and one winglet pair
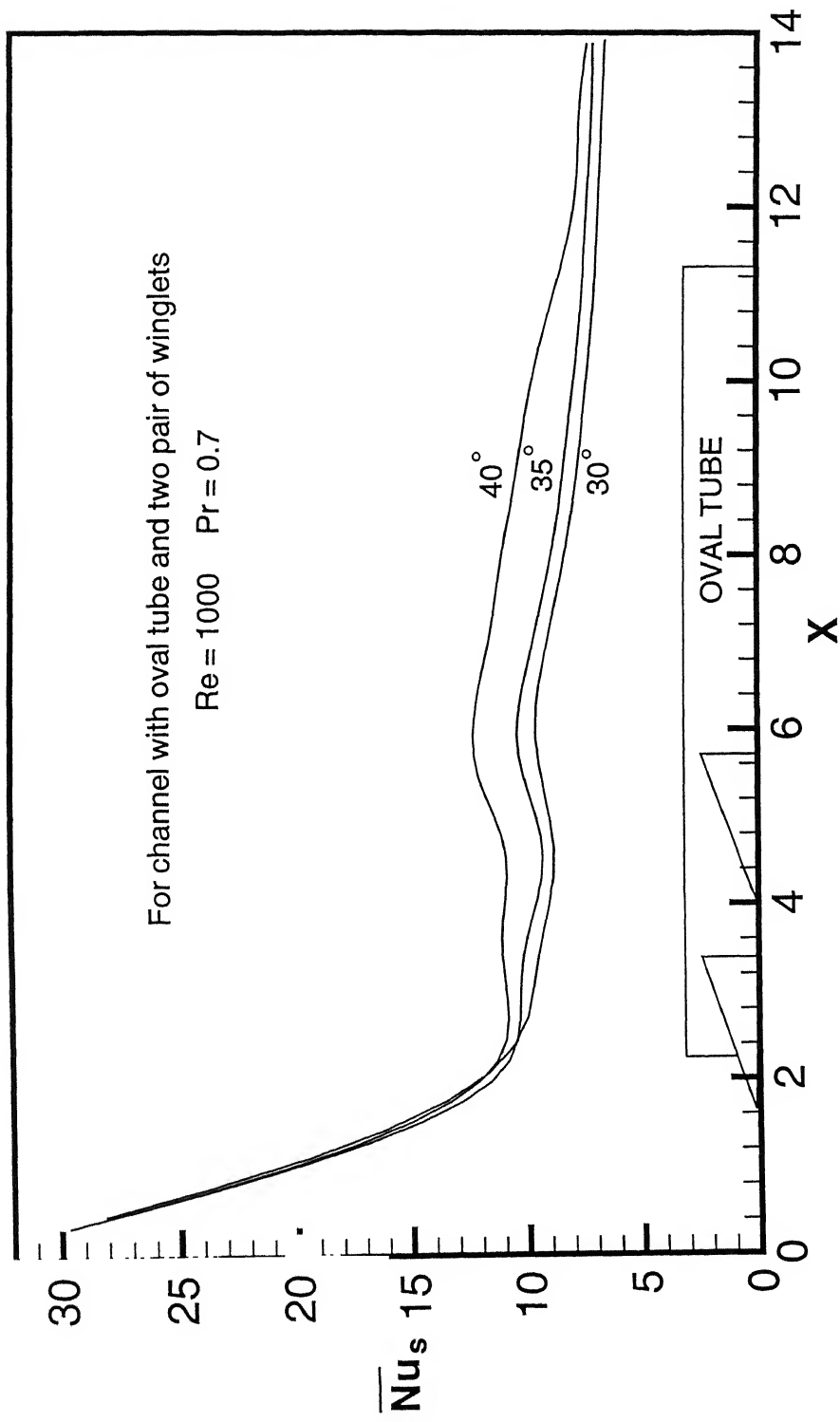
Figure 4.16   Comparison of span averaged Nusselt number for different angles of
attack for the case of flow through channel with oval tube and two winglet
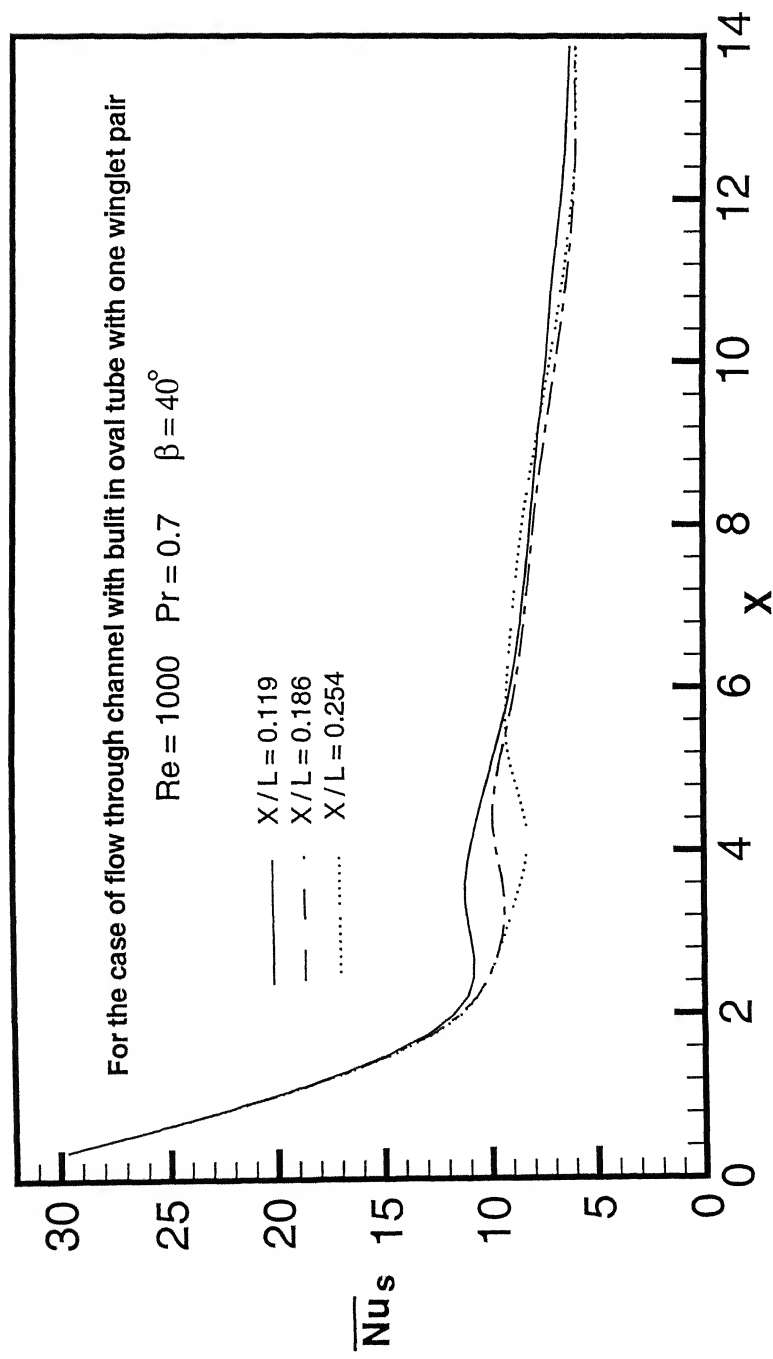pairs

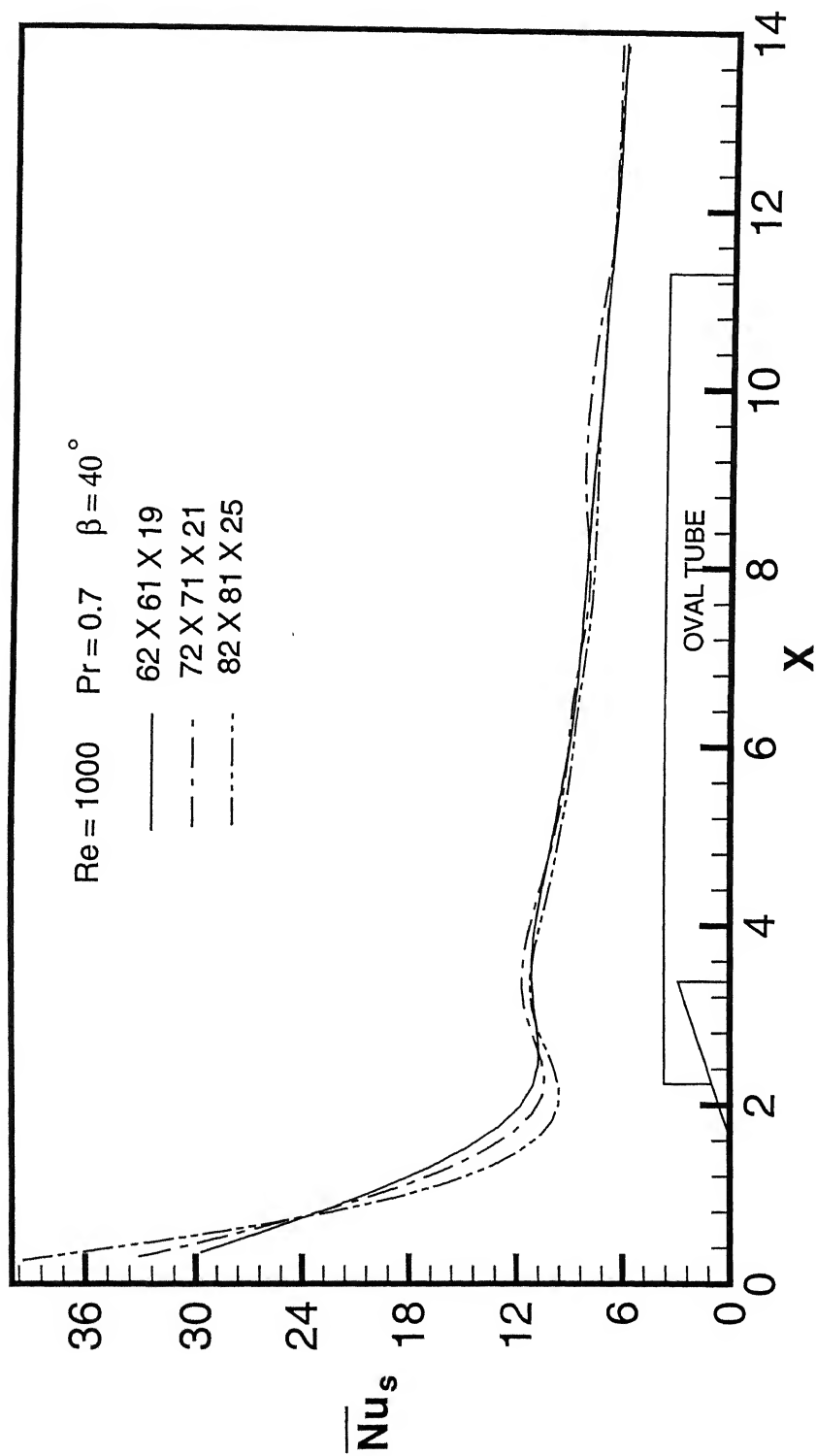Figure 4.17   Comparison of span averaged nusselt number for different axial locations of one pair of winglet

Figure 4.18   Grid independence test

Chapter 5
CONCLUSION AND SCOPE FOR FUTURE WORK

5.1 Conclusion

A three-dimensional computational study of forced convection heat transfer has been accomplished to determine the flow structure and heat transfer in a rectangular channel with built-in oval tube and delta winglet type vortex generators in common-flow-down or/ and common-flow-up configurations. The duct was designed to simulate a passage, formed by two neighboring fins in a fin-tube heat exchanger. A body-fitting grid has been used for simulation of flow and heat transfer and investigation has been carried out in full domain. The governing conservation equations for flow and heat transfer are expressed in integral form. An explicit control volume formulation due to Eswaran and Prakash (1998) is used to solve the governing equations. Limiting streamlines on the bottom wall have clearly shown the presence saddle point of separation, the nodal point of attachment and the horseshoe vortex system in front of the tube-bottom wall junction. The horseshoe vortices wrap around the tube and extend to the rear end of the tube. The enhancement of heat transfer is observed over the zone of influence of the horseshoe vortices. The additional longitudinal vortices are generated by the winglet pair. The main (primary) vortices and the corner (horseshoe) vortices produced by each winglet serve in creation of a strong swirling motion. The swirling motion disrupt the growth of thermal boundary layer and enhance the heat transfer keeping increase in pressure drop at a modest level. The mean span-averaged Nusselt number for a winglet pair with common-flow-down configuration is about 45 percent higher as compared to no-vortex generator case at a Reynolds number of 1000. This enhancement is 68.66 percent for the case of two winglet pairs, inner pair in common-flow-down and the outer pair in common-flow-up configuration. Enhancement of heat transfer is remarkable even at far downstream locations. Present study reveals that the

combination of oval tube and the winglet pair improves the heat transfer significantly. Since the oval tube and the winglet pair, both are streamline bodies, the pressure drop due to combination of the oval tube and the winglet pair vis-à-vis the pressure drop due to the circular tube are not expected to differ much.

5.2   Scope for Future Work

The results of this work establish the strategy of using oval tube and winglet pair in fin-tube heat exchangers as a useful technique for improving the heat transfer performance of the air-cooled condensers for geothermal power plants. Winglet pair can be mounted beside the oval tube in both, common-flow-down and common-flow-up configurations. It is evident that the winglet type vortex generators are capable of enhancing the heat transfer performance. However, the proper calculation of pressure penalty for each geometrical configuration has to be accomplished before embarking on a design change of the existing heat exchangers.

References

1. Biswas, G., Mitra, N. K. and Fiebig, M., (1989), Computation of Laminar Mixed Convection Flow in a Channel with Wing-type Built-in Obstacles, *J. Thermophysics and Heat Transfer (AIAA)*, Vol. 3, pp 447-453.

2. Biswas, G. and Chattopadhaya, H. (1992), Heat Transfer in a Channel with Built-in Wing-Type Vortex Generators, *Int. J. Heat Mass transfer*, Vol. 35, pp. 803-814.

3. Biswas, G., and Mitra, N. K. and Fiebig, M. (1994 a), Heat Transfer Enhancement in Fin-Tube Heat Exchangers by Winglet-Type Vortex Generators, *Int. J. Heat Mass Transfer*, Vol. 37, pp. 283-291.

4. Biswas, G., Deb, P., and Biswas, S., (1994 b), Generation of Longitudinal Streamwise Vortices - A Device for Improving Heat Exchanger Design, *Journal of Heat Transfer (ASME)*, Vol. 116, pp. 588-597.

5. Biswas, G., Torii, K., Fujii, D. and Nishino, K. (1996), Numerical and Experimental Determination of Flow Structure and Heat Transfer Effects of Longitudinal Vortices in a Channel Flow, *Int. J. Heat Mass Transfer*, Vol. 39, No. 16, pp. 3441-3451.

6. Cantwell, B. and Coles, D., (1983), An Experimental Study of Entrainment and Transport in the Turbulent Near Wake Circular Cylinder, *J. Fluid Mech.*, Vol. 136, pp. 321-374.

7. Chen, Y., Fiebig, M. and Mitra, N. K., (1998), Conjugate Heat Transfer of a Finned Oval Tube with a Punched Longitudinal Vortex Generator in form a Delta

Winglet-Parametric Investigations of the Winglet, *Int. J. Heat Mass Transfer*, Vol. 41, pp. 3961-3978.

8. Deb, P., Biswas, G. and Mitra, N.K. (1995), Heat Transfer and Flow Structure in Laminar and Turbulent Flows in a Rectangular Channel with Longitudinal Vortices, *Int. J. Heat Mass Transfer*, Vol. 38, pp. 2427-2444.

9. Eibeck, P.A. and Eaton, J.K. (1987), Heat Transfer of a Longitudinal Vortex Embedded in a Turbulent Boundary Layer, *Journal of Heat Transfer (ASME)*, Vol. 6, pp. 16-24.

10. Eswaran, V. and Prakash, S. (1998), A Finite Volume Method for Navier-Stokes Equations, *Proceedings of the third Asian CFD Conference, Bangalore*, Vol. 1, pp. 251-269.

11. Feigenbaum, M. J., (1980), The Onset Spectrum of Turbulence, *Phys. Lett.*, part-A, Vol. 74, pp. 375-378.

12. Ferziger, J. H., and Peric, M. (1999), *Computational Methods for Fluid Dynamics*, Springer Verlag, Berlin, New York.

13. Fiebig, M., Kallweit, P. and Mitra, N. K. (1986), Wing Type Vortex Generators for Heat Transfer Enhancement, *Proc. 8th IHTC*, Vol. 6, pp. 2909-2913.

14. Fiebig, M., Brockmeier, U., Mitra, N. K. and Guntermann, T. (1989), structure of Velocity and Temperature Fields in Laminar Channel Flows with Longitudinal Vortex Generators, *Numerical Heat Transfer*, Part A, Vol. 15, pp. 281-302

15. Fiebig, M., Dong, Y. and Mitra N.K. (1990), Warmeuberganangserhohung und Widerstandsverringerung durch Laenhgswirbelerzeuger in Rippenrohren, Waeme and Stoffubertragung, Vol. 25, pp. 34-44.

16. Fiebig, M., Kållweit, P., Mitra, N. K. and Tiggelbeck, S. (1991), Heat Transfer Enhancement and Drag by Longitudinal Vortex Generators in Channel Flow, *Experimental Thermal and Fluid Science*, Vol. 4, pp. 103-114.

17. Garg, V. K. and Maji, P. K. (1987), Flow through a Converging-Diverging Tube with Constant Wall Enthalpy, *Numerical Heat Transfer*, Vol. 12, pp. 285-305.

18. Guzmán, A. M. and Amon, C. H., (1996), Dynamical Flow Characterization of Transitional and Chaotic regimes in Converging-Diverging Channels, *J. Fluid Mech.*, Vol. 321, pp. 25-57.

19. Harlow, F. H., and Welch, J. E., (1965), Numerical Calculation of Time-dependent Viscous Incompressible Flow of Fluid with Free Surface, *The Phys. Fluids*, Vol. 8, pp. 2182-2188.

20. Hirt, C. W. and Cook, J. L. (1972), Calculating Three-Dimensional Flows Around Structures and Over Rough Terrain, *J. Comp. Phys.*, Vol. 10, pp. 324-340.

21. Karniadakis, G. and Triantafyllou, G., (1992), Three-Dimensional Dynamics and Transition to Turbulence in the Wake of Bluff Objects, *J. Fluid Mech.*, Vol. 238, pp. 1-30.

22. Khosla, P. K., and Rubin, S. G., (1974), A diagonally dominant second-order accurate implicit scheme, *Comp. & Fluids*, Vol. 2, pp. 207-209.

23. Kordulla, W., and Vinokur, M., (1983), Efficient Computation of Volume in Flow Predictions, *AIAA J.,* Vol. 21, No. 6, pp. 917-918.

24. Liou, T. M., Chen, C. C., and Tsai, T. W., (2000), Heat Transfer and Fluid Flow in a Square Duct with 12 Different Shaped Vortex Generators, *Journal of Heat Transfer (ASME),* Vol. 122, pp. 327-335.

25. Majumdar , S., Rodi, W., and Zhu, J., 1992, Three-Dimensional Finite-Volume Method for Incompressible flows with Complex Boundaries, *J. of Fluids Engg. (ASME)*, Vol. 114, pp. 496-503.

26. Majumdar, S. (1988), Role of Underrelaxation in Momentum Interpolation for calculation of Flow with Non-Staggered Grids, *Numerical Heat Transfer*, Vol. 13, pp. 125-132.

27. Manneville, P. and Pomeau, Y. (1980), Different ways to Turbulent in Dissipative Dynamical Systems, *Physica D*, Vol. 1, pp. 219-226.

28. Mendez, R. R., Sen, M., Yang, K. T. and McClain, R. L. (1998), Enhancement of Heat Transfer in an Inviscid-Flow Thermal Boundary Layer Due to a Rankine Vortex, *Int. J. Heat Mass Transfer*, Vol. 41, pp. 3829-3840.

29. O'Brien, J. E., and Sohal, M. S. (2000), Local Heat Transfer for Finned-Tube Heat Exchangers Using Oval Tubes, *Proceedings of NHTC'00, 34th National Heat Transfer Conference*, Pittsburgh, Pennsylvania, USA.

30. Orlanski, I. (1976), A Simple Boundary Condition for Unbounded Flows, *J. Comp. Phys*, Vol. 21, pp. 251-269.

31. Patankar, S. V. and Spalding, D. B. (1972), A Calculation Procedure for Heat Mass and Momentum Transfer in three-Dimensional Parabolic Flows, *Int. J. Heat Mass Transfer*, Vol. 15, pp. 1787-1806.

32. Pauley, W. R. and Eaton, J. K. (1988), Experimental Study of the Development of Longitudinal Vortex pairs Embedded in a Turbulent Boundary Layer, *AIAA J.*, Vol. 26, pp. 816-823.

33. Peric, M. (1985), A Finite Volume Method for the Prediction Of Three-Dimensional Fluid Flow in Complex Ducts, *Ph. D. Thesis*, University of London.

34. Peric, M., Kessler, R. and Scheuerer, G. (1988), Comparison of Finite-Volume Numerical Methods with a Staggered and Collocated Grids, *Computers & Fluids*, Vol. 16, pp. 389-403.

35. Perry, A.E., Chong, M. S. and Lim, T. T., (1982), The Vortex-Shedding Progress Behind Two-Dimensional Bluff Bodies, *J. Fluid Mech.*, Vol. 116, pp. 77-90.

36. Prabhakar, V., Biswas, G. and Eswaran, V. (2001) Numerical Prediction of Heat Transfer in a Channel with a Built-in Oval Tube and Two Different Shaped Vortex Generators, *Numerical Heat Transfer*, Part-A (accepted for publication).

37. Ruelle, D. and Takens, F., (1971), On the Nature of turbulence, *Commun. Math. Phys.*, Vol. 20, pp. 167-192.

38. Rhie, C. M. and Chow, B. L. (1983), Numerical Study of Flow Past an Aerofoil with Trailing Edge Separation, *AIAA J.*, Vol. 21, pp. 1525-1532.

39. Rhie, C. M. (1981), A Numerical Study of the Flow Past an Isolated Airflow with Separation, Ph.D. Thesis, Dept. of Mechanical and Industrial Engg., University of Illinios at Urbana Champaign, 1981.

40. Roshko, A., (1993), Perspectives on Bluff Body Aerodynamics, *J. Wind Engg. Ind. Aerodyn.*, Vol. 49, pp. 79-100.

41. Tiggelbeck, S., Mitra, N. K., and Fiebig, M., (1994), Comparison of Wing Type Vortex Generators for Heat Transfer Enhancement in Channel Flows, *Journal of Heat Transfer (ASME)*, Vol. 116, pp 880-885.

42. Torii, K., Nishino, K., and Nakayama, K., (1994), Mechanism of Heat Transfer Augmentation by Longitudinal Vortices in a Flat Plate Boundary Layer, *Pro. Tenth Int. Heat Transfer Conference*, Vol. 6, pp. 123-128.

43. Valencia, A., Fiebig, M., and Mitra, N. K., (1996) Heat Transfer Enhancement by Longitudinal Vortices in Fin-Tube Heat Exchanger Element with Flat Tubes, *Journal of Heat Transfer (ASME)*, Vol. 118, pp 209-211.

44. Van Doormal, J. P., and Raithby, G. D., (1984), Enhancement of SIMPLE method of Predicting Incompressible Fluid Flows, *Numerical Heat Transfer*, Vol. 7, pp 147-163.

45. Vasudevan, R., Eswaran, V., and Biswas, G., (2000), Winglet-Type Vortex Generators for Plate-Fin Heat Exchangers using Triangular Fins, *Numerical Heat Transfer*, Part A, Vol. 38, pp. 533-555.

46. Velusamy, K. and Garg, V. K. (1993), Entrance Flow in Elliptic Ducts, *Int. J. Numerical Methods Fluids*, Vol. 17, pp. 1079-1096.

47. Vittori, G. and Blondeaux, P. (1993), Quasiperiodicity and Phase Locking Route to chaos in the Two-Dimensional Oscillatory Flow Around a Circular Cylinder, *Phys. Fluids*, Part-A, Vol. 5, pp. 1866-1868.

48. Westphal, R. V., and Mehta, R. D., 1987, Interaction of Oscillating Vortex with a Turbulent Boundary layer, *AIAA 19th Fluid Dynamics and Laser Conference*, Hawaii, AIAA paper no. 87-1246.

49. Yanagihara, J. L. and Torii, K., (1990), Heat Transfer characteristics of Laminar Boundary Layer in the Presence of Vortex Generators, *Proc. 9th IHTC*, Vol. 6, pp. 323-328.